Unsteady Aeroservoelastic Modeling of Flexible Wing Generic Transport Aircraft with Variable Camber Continuous Trailing Edge Flap

Ezra Tal[*]

Delft University of Technology, Delft, 2629 HS, Netherlands

Nhan Nguyen[†]

NASA Ames Research Center, Moffett Field, CA 94035

This paper presents a coupled flight dynamic and aeroservoelastic model of the NASA Generic Transport Model with increased wing flexibility and a continuous trailing edge flap system. The continuous trailing edge flap consists of multiple segments that are connected using a flexible skin material. Dynamic models of the aircraft, flexible wing, and flap system are aerodynamically coupled. Aerodynamics of the aircraft are modeled using a 3D vortex-lattice method. Unsteady aerodynamics of the flexible wing and flap system are modeled using modified strip theory based on quasi-steady vortex-lattice results and indicial concepts with unsteady aerodynamic corrections. The frequency-independent aeroelastic state-space system is formulated by means of aerodynamic lag states. A method for the realization of spatial turbulence and its application to flight dynamic simulation of flexible aircraft are described. The unsteady gust responses of the elastic aircraft and the flap system are also modeled using an indicial function approximation of the unsteady aerodynamic response. Compressibility effects on the unsteady aerodynamics are taken into account throughout the modeling effort using methods by Beddoes and Leishman et al. and a comparison is made with unsteady aerodynamics in incompressible flow. Simulation results, including flight dynamic and elastic responses, and aerodynamic hinge moments, are shown for flight dynamic maneuvers and gust profiles.

I.   Introduction

In pursuit of energy efficient airframe designs, the aircraft industry is utilizing modern lightweight materials, such as sophisticated composites, at increasing scale. Such materials may be able to provide sufficient load-carrying capacity at lower weight, leading to reduction of the aircraft operational empty weight (OEW). At the same time application of these materials may lead to decreased structural rigidity. With increased flexibility of the airframe, aeroelastic effects become more prominent and can significantly affect aircraft performance and stability, potentially leading to degraded aerodynamic efficiency and decrease of control surface effectiveness.

Under the Fundamental Aeronautics Program of the NASA Aeronautics Research Mission Directorate (ARMD), the Fixed Wing/Advanced Air Transport Technology Project is conducting multidisciplinary foundational research to investigate advanced concepts and technologies for future aircraft systems. A NASA study entitled "Elastically Shaped Future Air Vehicle Concept" was conducted in 2010[1,2] to examine new concepts that can enable active control of wing aeroelasticity to achieve drag reduction. This study showed that highly flexible wing aerodynamic surfaces can be elastically shaped in-flight by active control of wing twist and vertical deflection in order to optimize the local angle of attack of wing sections to improve aerodynamic efficiency through drag reduction during cruise and enhanced lift performance during take-off and landing. For the purpose of aeroelastic shaping control, a continuous flap system called the Variable Camber Continuous Trailing Edge Flap (VCCTEF) was introduced.

---

[*]Graduate Student, Faculty of Aerospace Engineering, e.a.tal@student.tudelft.nl, AIAA Student Member
[†]Research Scientist, Intelligent Systems Division, nhan.t.nguyen@nasa.gov, AIAA Associate Fellow

American Institute of Aeronautics and Astronautics

As aircraft structures become increasingly flexible and aeroelastic effects become more prominent, a representation of flight characteristics based on a rigid-body six degrees of freedom (6DOF) flight dynamic model becomes inadequate. Structural dynamics of the aircraft are intimately coupled with flight dynamics and must be accounted for in the modeling of flexible flight vehicles. Additionally, aeroservoelastic interactions demand consideration in the control design. The mishap of the NASA Helios aircraft illustrates the complex aeroservoelasticity of flexible flight vehicles.[3] The need to assess flight performance and handling qualities and the need to design and simulate flight control systems call for coupled flight dynamic and aeroservoelastic modeling of flexible flight vehicles.

In general, the coupled equations of motion are dependent on the reduced frequency parameter. This form is very useful for studying flutter since the reduced frequency is usually computed from a flutter solution. However, for flight dynamic analysis, the reduced frequency dependent equation is inconvenient, since one would not know in advance which elastic modes are excited. Random gust loads, flight dynamic maneuvers, and high-bandwidth control may cause the excitation of multiple modes at a range of different frequencies. A reduced frequency-dependent formulation may only be based on a single preselected frequency, leading to misrepresentation of the aeroelastic modes acting at different frequencies. In order to address this difficulty, a frequency-independent approach based on modified aerodynamic strip theory is used to model the unsteady aerodynamics of the elastic wing and VCCTEF. The solution employs 2D unsteady indicial functions combined with 3D quasi-steady vortex-lattice results. The indicial functions include unsteady compressibility effects, in contrast to the well-known Theodorsen's function for incompressible flow.[4] This approach permits the development of an unsteady aerodynamic model including unsteady compressibility effects at a fraction of the computational cost of an unsteady solution obtained using Computational Fluid Dynamics (CFD).

In addition to unsteady aerodynamics, several other aspects of coupled flight dynamic and aeroservoelastic modeling are addressed. The VCCTEF structural model is developed and a spatial turbulence model with corresponding unsteady aerodynamic response model is shown. Simulation results, including flight dynamic and elastic responses, and aerodynamic hinge moments, are shown for flight dynamic maneuvers and gust profiles.

II. Overview of Elastically Shaped Aircraft Concept and Variable Camber Continuous Trailing Edge Flap

The Elastically Shaped Aircraft Concept (ESAC) is modeled as a notional single-aisle, mid-size, 200-passenger aircraft. The geometry of the ESAC is obtained by scaling up the geometry of the NASA Generic Transport Model (GTM) by a ratio of 200:11. The GTM is a research platform that includes a wind tunnel model and a remotely piloted vehicle, as shown in Figure 1. Figure 2 is an illustration of the GTM geometry. The reason for selecting the GTM is that there already exists an extensive wind tunnel aerodynamic database that could be used for validation in the study. The benchmark configuration represents one of the most common types of transport aircraft in the commercial aviation sector that provides short-to-medium range passenger carrying capacities.

The aircraft has a take-off weight of 200,000 lbs for a typical operating load that includes cargo, fuel, and passengers. To compute the mass and inertia properties of the benchmark aircraft, a component-based approach is used. The aircraft is divided into the following components: fuselage, wings, horizontal tails, vertical tail, engines, OEW equipment, and typical load including passengers, cargo, and fuel. The fuselage, wings, horizontal tails, and vertical tail are modeled as shell structures with constant wall thicknesses. Based on publicly available data of component weight breakdown for various aircraft,[5] an average wing mass relative to the total empty weight of the aircraft is taken to be 24.2% of the OEW.

To enable active wing shaping control, the wing structures of the ESAC are designed to increase wing flexibility. The wing bending and torsional stiffnesses are designed to achieve a wing deflection that is about double of that of a conventional aircraft wing. The VCCTEF consists of 15 sections attached to the outer wing and one section attached to the inner wing, as shown in Figure 3. Each section has three camber flap segments that can be individually commanded, as shown in Figure 4. These camber flaps are joined to the next section by a flexible and supported material of same shape as the camber and thus providing continuous flaps throughout the wing span with no drag producing gaps.

Using the camber positioning, a full-span, low-drag, high-lift configuration can be activated. The camber positioning is achieved using all three flap segments. The leading two segments are actuated by means of a

American Institute of Aeronautics and Astronautics

Figure 1: Generic Transport Model and Remotely Piloted Vehicle at NASA Langley

Figure 2: GTM Geometry

American Institute of Aeronautics and Astronautics

shape memory alloy, while the trailing edge segments are actuated using a fast electro-mechanical actuator and can therefore also be applied for flight dynamic maneuvers and high-bandwidth control purposes, such as flutter suppression and gust alleviation. The bandwidth of the shape memory alloy actuator is several orders of magnitude lower than the bandwidth of the electro-mechanical actuator. Due to separation of timescales, the modeling of the leading two segments is less relevant from a flight dynamic and aeroservoelastic point of view, hence the model discussed in this paper only includes the dynamics of the fast-acting trailing edge segments. The effect of the first two segments is assumed constant and can be included in the static wing geometry.
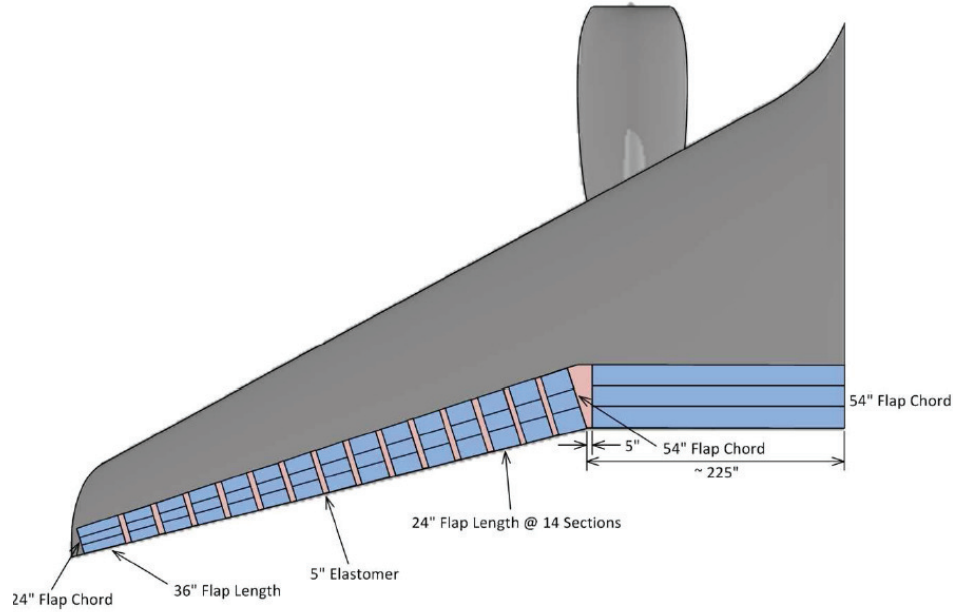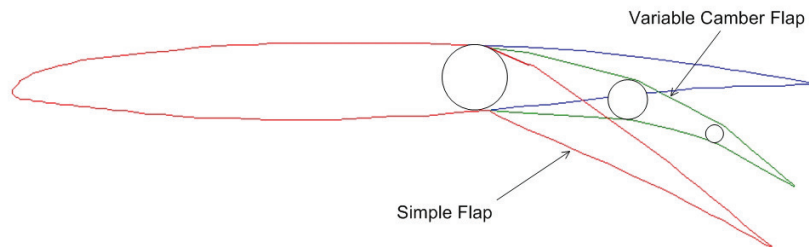

Figure 3: GTM with VCCTEF

Figure 4: Variable Camber Flap

III.   Flight Dynamics

The basis of the flight dynamic model is a nonlinear rigid-body flight dynamic model of the GTM incorporating the well-known 6DOF nonlinear flight dynamic and kinematic equations. Stability and control derivatives were obtained using a vortex-lattice code. Multivariate splines were fitted to the stability and control derivatives in order to enable computationally efficient evaluation during simulation. For system

American Institute of Aeronautics and Astronautics

analysis and control design purposes, it can be useful to couple the linearized flight dynamic equations to the aeroservoelastic system. Linearization can be performed analytically or using numerical methods, such as the finite difference method. For this study both a numerical linearization and the analytical coupled linear flight dynamic equations of motion[6] were implemented.

The coupling of aeroelasticity and rigid-body dynamics must be accounted for in order to trim the aircraft to a steady flight condition. This is done by concurrently calculating the steady-state wing deflection and corresponding aeroelastic forces and moments within the trim routine.

IV.   Elastic Wing Dynamics

In previous work an FEM model of the elastic wing was developed.[7] The model is based on an equivalent beam approach and has three degrees of freedom: vertical displacement, flapwise bending, and twist. Horizontal displacement and chordwise bending can be neglected, as the stiffness of the ESAC wing is far greater in chordwise direction.

Inertial, propulsive, structural, and aerodynamic forces and moments are taken into account. The derivation of the aerodynamic forces and moments in the streamwise coordinate frame is based on modified strip theory.

The local lift force and pitching moment about the aircraft y-axis along the elastic axis are expressed as

$$l(x) = \left(c_L^c(x) + c_L^{nc}(x) + c_L^{c,\delta}(x) + c_L^{nc,\delta}(x) \right) q_\infty \cos \Lambda c(x) \tag{1}$$

$$m(x) = \left(c_m^c(x) + c_m^{nc}(x) + c_m^{c,\delta}(x) + c_m^{nc,\delta}(x) \right) q_\infty \cos \Lambda c(x)^2 \tag{2}$$

where the superscripts c and nc indicate respectively circulatory and noncirculatory contributions by the aircraft rigid body and the elastic wing, and the superscripts c, δ and nc, δ indicate respectively circulatory and noncirculatory contributions by the VCCTEF. These are not only a function of the flap angles δ, but also depend on their derivatives, as shown in Section V.

The noncirculatory contributions result from the change in momentum of surrounding air due to the motion of the airfoil and flap. Also due to the airfoil and flap motion, the circulation in the bound vortex changes and by Kelvin's circulation theorem, an equal but opposite amount of circulation is added to the wake vortex. The increment in wake circulation induces a velocity increment at the airfoil, resulting in a phase lag and decrease in magnitude of the circulatory lift relative to the steady-state value for the same angle of attack.

For incompressible flow, an expression for the effect of phase lag and decrease in magnitude as a function of the reduced frequency k of a harmonically oscillating airfoil is given by Theodorsen's function[4]

$$C(k) = F(k) + iG(k) \tag{3}$$

where $F(k) \geq 0.5$, $G(k) \leq 0$, and

$$k = \frac{\omega c}{2V} \tag{4}$$

with ω the oscillation frequency, c the airfoil chord, and V the free stream airspeed. The functions $F(k)$ and $G(k)$ are analytically defined in terms of Bessel functions.[4] Existing work extends the application of Theodorsen's function to airfoils in arbitrary motion.[8, 9]

The time-domain equivalent of Theodorsen's function is given by Wagner's indicial function,[10] which gives the lift response to a step change in angle of attack and forms a Fourier transform pair with Theodorsen's function. Wagner's function is also analytically defined and expressed in terms of Bessel functions. In case of arbitrary airfoil motion, such as in flight dynamic simulations, it can be applied to calculate forces and moments by virtue of Duhamel's integral.

Function approximations are often resorted to for practical application of Theodorsen's or Wagner's function. Rational fraction approximations may be used in case of Theodorsen's function in the frequency-domain[11, 12] and exponential time-domain approximations in case of Wagner's function. The most well-known of these exponential approximations is given by R.T. Jones,[13] namely

$$\phi(S) = 1 - 0.165e^{-0.0455S} - 0.335e^{-0.3S} \tag{5}$$

where $S = \frac{2V}{c}t$ is the distance traveled in semichords, after the step angle of attack change. The second-order approximation is able to capture the dynamics of Wagner's and Theodorsen's functions quite well. Increasing the order of approximation will generally increase accuracy, up to third-order beyond which accuracy gains are diminishing.[12] A major benefit of the exponential approximation is that its state-space representation can be realized straightforwardly.

As mentioned above, Theodorsen's function is valid only under the assumption of incompressible flow. Naturally, the same is the case for Wagner's function. A compressibility scaling, e.g. by the inverse Prandtl-Glauert factor, does not apply to the transient circulatory force and moment responses in unsteady aerodynamic conditions. Steady-state values are reached at a later time in the compressible case, as compared to the incompressible case.[14]

For incompressible flow, the noncirculatory force and moment contributions due to apparent mass are instant and not subject to a time-history effect.[4] This is not applicable to compressible flow as the speed of sound is now considered finite and pressure disturbances are not felt instantly.[14] Instead, the noncirculatory forces and moments are subject to a time-history effect, similar to their circulatory counterparts.

Modeling of compressible unsteady aerodynamics is generally more complicated and there are no analytical solutions, such as for the incompressible case.[15] Analytic indicial lift and moment functions can only be derived for a small time range following an angle of attack or pitch rate step input. In order to do so Lomax utilizes the analogy between a two-dimensional wing in unsteady motion and a three-dimensional lifting surface in steady motion.[16] Asymptotic steady-state values are not yet approached at the end of this range. Hence, an expression for the intermediate behavior remains to be found. This problem has been approached in several ways, e.g. using experimental data[17] and using computational methods.[18]

Beddoes proposes a method of describing the unsteady compressible forces and moments by approximations based on a combination of numerical and analytical solutions. An exponential form is assumed, similar to the form of R.T. Jones' approximation for circulatory lift.

For noncirculatory lift, an approximation by a decreasing function consisting of a single exponential term is assumed. This form can approach the time-dependent behavior of solutions for the noncirculatory lift component, such as those based on the acoustic approximation,[19] quite well. From a flight dynamic modeling point of view, the exponential approximation is much more convenient than the solution of the acoustic approximation, which is formulated in terms of Mathieu functions.

Beddoes makes use of the analytical solution for the initial part of the response as derived by Lomax[16] in order to determine the time constant of the noncirculatory lift approximation. The time derivative of the analytical total lift function at $S = 0$ is equated to the sum of the time derivatives of the approximations for the circulatory and noncirculatory lift contributions. The method has been applied and further developed by Leishman and Nguyen[20] and was validated using experimental data.[21] Using a combination of linear unsteady theory and aerodynamic reverse-flow theorems, similar approximations for a flapped airfoil were also developed.[22] A convenient overview of approximations with state-space realizations is given by Leishman and Nguyen,[20] and by Hariharan and Leishman.[22] These approximations are applied in the present study. An overview is given below.

A.   Aerodynamic Forces and Moments due to Elastic Wing

The aerodynamic forces and moments on the elastic wing due to aircraft geometry, static and dynamic deformations and deformation rates of the elastic wing, and aircraft rigid-body orientation and motion are calculated using the notion of a local aeroelastic angle of attack. This angle of attack is a measure of the total local upwash relative to the wing section and includes contributions by all of the aforementioned states.[7]

The sectional unsteady aerodynamic lift force and pitching moment consist of circulatory and noncirculatory contributions. Aerodynamic lag states are applied in order to model the time-dependent effects of these contributions. The aerodynamic lag states are driven by the local aeroelastic angle of attack and the local (sectional) pitch rate. As mentioned above, the local angle of attack and local pitch rate generally include contributions by both the rigid body and elastic wing orientation and motion. However, for the purpose of coupling the elastic wing to the nonlinear rigid-body dynamics in the current study it is necessary to separate rigid-body and elastic wing contributions. Hence, the rigid-body contribution is assumed quasi-steady and not incorporated in the aerodynamic lag states. This assumption is admissible due to the relatively low frequency of the rigid-body dynamics.

Eight aerodynamic lag states are required to model the 2D circulatory and noncirculatory lift force and pitching moment due to the elastic wing. Consequently, the total number of aerodynamic lag states in the

full-order model is equal to ten times the number of aerodynamic strips. The aerodynamic lag state dynamics are given below.

Where available the circulatory force and moment derivatives with regard to the aeroelastic angle of attack are taken from a quasi-steady vortex-lattice code. These values are indicated by the superscript QS.

The aerodynamic lag state dynamics are based on indicial response functions that model the lift and pitching moment response due to a step angle input, similar to Wagner's function for incompressible flow, or a step pitch rate input. The motion of the wing section is described in terms of the angle of attack at the quarter chord point, $\alpha_{1/4}$, and the pitch rate at the same point and normalized by $\frac{c}{V}$, $q_{1/4}$. Together these parameters can be used to describe any chordwise linear upwash profile due to pitch and plunge motion of the wing section. The upwash at the quarter chord point is determined by $\alpha_{1/4}$ and any chordwise linear variation by $q_{1/4}$.

The indicial functions consist of exponential terms, hence a state-space realization can easily be derived. The circulatory lift response to a unit angle of attack step input is given by

$$c_L^c = c_{L_\alpha}^{QS} \alpha_{3/4} \left(1 - a_1 e^{-b_1 \beta^2 S} - a_2 e^{-b_2 \beta^2 S} \right) \tag{6}$$

where $a_1 = 0.3$, $a_2 = 0.7$, $b_1 = 0.14$ and $b_2 = 0.53$ as given by Beddoes,[18] $\beta = \sqrt{1 - M^2}$ is the Prandtl-Glauert correction factor, and $c_{L_\alpha}^{QS}$ is the quasi-steady lift slope obtained from vortex-lattice calculations. The angle of attack at the three quarter chord location, $\alpha_{3/4}$, is given by

$$\alpha_{3/4} = \alpha_{1/4} + \frac{q_{1/4}}{2} \tag{7}$$

By examination of equation (6) similarity to the form of R.T. Jones' approximation, equation (5), can easily be observed. It can also be seen that c_L^c asymptotically approaches its quasi-steady value if $\alpha_{3/4}$ is constant. Similar to Theodorsen's expression, the circulatory lift is dependent on the angle of attack at the three quarter chord point.

The state-space equivalent of equation (6) is realized using two aerodynamic lag states. The resulting system of differential equations is given by

$$\dot{x}_1 = - \left(\frac{2V}{c} \right) \beta^2 b_1 x_1 + \alpha_{3/4} \tag{8}$$

$$\dot{x}_2 = - \left(\frac{2V}{c} \right) \beta^2 b_2 x_2 + \alpha_{3/4} \tag{9}$$

where c is the local chord length. The local circulatory lift coefficient due to elastic wing deformation is then given by

$$c_L^c = c_{L_\alpha}^{QS} \left(\frac{2V}{c} \right) \beta^2 \left(a_1 b_1 x_1 + a_2 b_2 x_2 \right) \tag{10}$$

For brevity purposes, the exponential forms of the remaining indicial functions for noncirculatory lift, and noncirculatory and circulatory pitching moment are not given here. They can however straightforwardly be derived from the shown state-space realizations or found in references.[20, 22]

For the noncirculatory lift due to angle of attack, a single lag state is used

$$\dot{x}_3 = -\frac{1}{K_\alpha T_I} x_3 + \alpha_{1/4} \tag{11}$$

where $T_I = \frac{c}{a}$ with a the speed of sound and K_α is to be determined in the subsequent analysis. The corresponding output equation is given by

$$c_L^{nc,\alpha} = \frac{4}{M} \dot{x}_3 \tag{12}$$

The speed of sound is considered infinite in incompressible flow, leading to $T_I = 0$. This effectively removes the time-dependent effect in equation (11). Concurrently, the Mach number is considered zero, consequently equation (12) becomes unbounded. The outcome is an instantaneous, unbounded, impulse-shaped noncirculatory lift output at $S = 0$ due to an angle of attack step input in incompressible flow. This corresponds to Theodorsen's formulation, where the noncirculatory lift due to an angle of attack step input is proportional to the time-derivative of the step input function, i.e. the Dirac delta function.

American Institute of Aeronautics and Astronautics

The time constant K_α is found by equating the time derivatives of the analytical and approximate solutions for a unit step angle of attack input at $S = 0$

$$\frac{\mathrm{d}c_L^\alpha(0)}{\mathrm{d}S} = \frac{\mathrm{d}c_L^c(0)}{\mathrm{d}S} + \frac{\mathrm{d}c_L^{nc,\alpha}(0)}{\mathrm{d}S} \tag{13}$$

Note that

$$\mathrm{d}S = \frac{2V}{c}\,\mathrm{d}t \tag{14}$$

so that from equations (8), (9), and (10)

$$\frac{\mathrm{d}c_L^c(0)}{\mathrm{d}S} = c_{L_\alpha}^{QS}\beta^2(a_1 b_1 + a_2 b_2) \tag{15}$$

and from equations (11) and (12)

$$\frac{\mathrm{d}c_L^{nc,\alpha}(0)}{\mathrm{d}S} = \frac{-4}{MK_\alpha T_I}\frac{c}{2V} \tag{16}$$

From the analytical solution[16] it is known that

$$\frac{\mathrm{d}c_L^\alpha(0)}{\mathrm{d}S} = \frac{-2\,(1-M)}{M^2} \tag{17}$$

By equating the time derivatives the expression for K_α can now be found

$$K_\alpha = \frac{2}{2\,(1-M) + c_{L_\alpha}^{QS}\beta^2 M^2\,(a_1 b_1 + a_2 b_2)} \tag{18}$$

In order to achieve agreement with test data, the noncirculatory time constants must sometimes be adapted from their theoretical values.[20,21] In the current study, the values were kept as followed from their respective derivations shown here.

The noncirculatory lift due to pitch rate at the quarter chord point is given by

$$\dot{x}_4 = -\frac{1}{K_q T_I}x_4 + q_{1/4} \tag{19}$$

and

$$c_L^{nc,q} = \frac{1}{M}\dot{x}_4 \tag{20}$$

The time constant K_q is found in a similar manner as K_α, and is defined as

$$K_q = \frac{1}{(1-M) + c_{L_\alpha}^{QS}\beta^2 M^2\,(a_1 b_1 + a_2 b_2)} \tag{21}$$

The pitching moment coefficient is taken about the quarter chord point. This is done in order to maintain the notations as used by Beddoes,[18] and Leishman and Nguyen.[20] The pitching moment about the quarter chord is primed to distinguish it from the pitching moment coefficient about the elastic axis location in equation (2).

It should be noted that the formulation of lift and pitching moment as a function of the angle of attack and pitch rate at the quarter chord point does not intrinsically lead to incompatibility with the formulation by Theodorsen. The instantaneous noncirculatory lift, for example, is based on the angle of attack at the mid-chord point in Theodorsen's formulation. Examination of the ratio of the output coefficients of equations (12) and (20) shows that the total instantaneous noncirculatory lift is again a function of the angle of attack at the mid-chord point, even though it consists of two separate contributions in the compressible formulation.

The circulatory pitching moment about the sectional quarter chord point due to angle of attack can be calculated from the circulatory lift and is given by

$$c_m^{c,\alpha\prime} = c_L^c\left(\frac{1}{4} - x_{ac}\right) \tag{22}$$

where x_{ac} is the distance of the aerodynamic center from the leading edge measured in chord lengths.

The noncirculatory pitching moment due to angle of attack is given by[21]

$$\dot{x}_5 = -\left(b_3 K_{\alpha_M} T_I\right)^{-1} x_5 + \alpha_{1/4} \tag{23}$$

$$\dot{x}_6 = -\left(b_4 K_{\alpha_M} T_I\right)^{-1} x_6 + \alpha_{1/4} \tag{24}$$

and

$$c_m^{nc,\alpha}\prime = -\frac{1}{M}\left(-a_3\left(b_3 K_{\alpha_M} T_I\right)^{-1} x_5 - a_4\left(b_4 K_{\alpha_M} T_I\right)^{-1} x_6\right) - \frac{1}{M}\alpha_{1/4} \tag{25}$$

where $a_3 = 1.5$, $a_4 = -0.5$, $b_3 = 0.25$, $b_4 = 0.1$, and the noncirculatory time constant

$$K_{\alpha_m} = \frac{a_3 b_4 + a_4 b_3}{b_3 b_4 \left(1 - M\right)} \tag{26}$$

The two remaining contributions are the circulatory and noncirculatory pitching moment due to pitch rate about the quarter chord point. The circulatory contribution is approximated by[20]

$$\dot{x}_7 = -b_5 \beta^2 \frac{2V}{c} x_7 + q_{1/4} \tag{27}$$

and

$$c_m^{c,q}\prime = -\frac{\pi}{16}\beta\frac{2V}{c} x_7 \tag{28}$$

where $b_5 = 0.5$. The noncirculatory contribution is approximated by[20]

$$\dot{x}_8 = -\frac{1}{K_{q_M} T_I} x_8 + q_{1/4} \tag{29}$$

and

$$c_m^{nc,q}\prime = -\frac{7}{12M}\dot{x}_8 \tag{30}$$

where the time constant is given by[20]

$$K_{q_m} = \frac{7}{15\left(1 - M\right) + 3\pi\beta M^2 b_5} \tag{31}$$

The total lift and pitching moment can now be obtained by summation of contributions:

$$c_L^c = c_L^c \tag{32}$$

$$c_L^{nc} = c_L^{nc,\alpha} + c_L^{nc,q} \tag{33}$$

$$c_m^c\prime = c_m^{c,\alpha}\prime + c_m^{c,q}\prime \tag{34}$$

$$c_m^{nc}\prime = c_m^{nc,\alpha}\prime + c_m^{nc,q}\prime \tag{35}$$

The pitching moment about the aircraft y-axis at the elastic axis location is given by

$$c_m^c = c_m^c\prime + e c_L^c \tag{36}$$

$$c_m^{nc} = c_m^{nc}\prime + e c_L^{nc} \tag{37}$$

where e is the distance of the elastic center back from the quarter chord point measured in chord lengths.

B.   Comparison to Incompressible Unsteady Aerodynamics

In order to compare the circulatory lift due to the angle of attack at the three quarter chord point, equation (6) is transformed to the frequency domain. The resulting frequency response function for Mach 0.797 is shown in Figure 5 along with Theodorsen's function, equation (3). Both functions are normalized using the steady-state value.
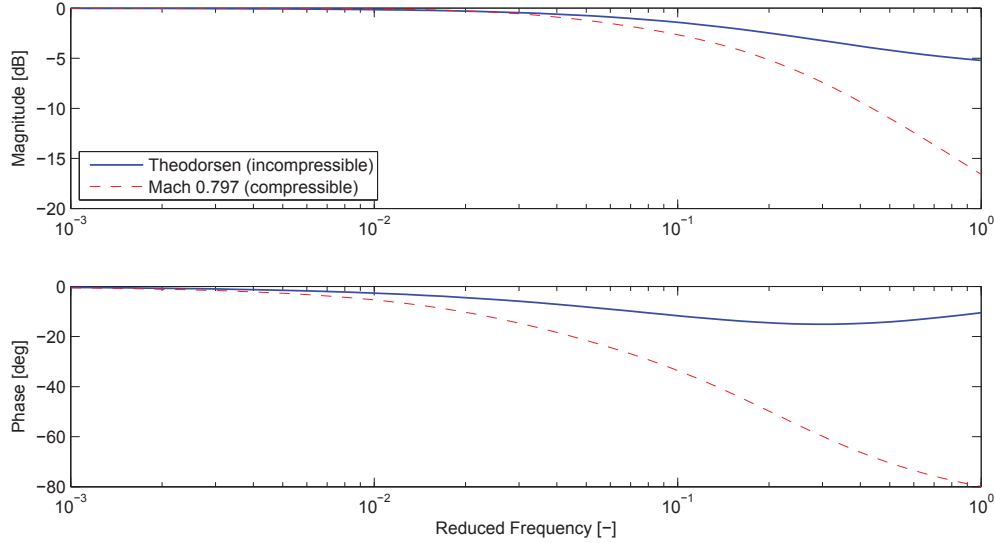
Figure 5: Circulatory lift due to harmonic variation of angle of attack at three quarter chord point

A major difference can immediately be observed at high frequencies, where the lift in compressible flow is zero, while the lift in incompressible flow has a magnitude of -6 dB (half of its steady-state value). This can also be observed when comparing equations (5) and (6) at $S = 0$. The initial value of zero for $S = 0$ in (6) is in agreement with the analytical compressible flow solution for small values of S by Lomax.[16]

In order to gain further insight in the differences between the expressions from the previous section and the results obtained by Theodorsen for the incompressible case, both are applied to a two-dimensional 2DOF wing profile. The wing profile has pitch and plunge degrees of freedom. Its aerodynamic and structural properties are equivalent to the sectional properties of the ESAC wing at two thirds of its span. The equations of motion are given by

$$m\ddot{h} + S_\theta\ddot{\theta} + K_h h = -L \tag{38}$$

$$S_\theta\ddot{h} + I_\theta\ddot{\theta} + K_\theta\theta = M \tag{39}$$

where m is the mass I_θ is the rotational inertia, and K_h and K_θ are vertical and rotational stiffness, respectively. The static mass moment, S_θ, accounts for the offset between elastic axis and center of gravity. The aerodynamic lift force, positive upward, is indicated by L and the pitching moment by M. The degrees of freedom are defined in Figure 6. Note that no structural damping is added to the 2DOF model. This is also the case for the ESAC model.

Using the expressions by Theodorsen,[4] the lift and pitching moment coefficients of an oscillating airfoil with two degrees of freedom can be formulated as

$$c_L = \frac{c}{2V}\left(\pi\dot{\theta} + \pi\frac{\ddot{h}}{V} - \pi a\frac{c}{2V}\ddot{\theta}\right) + c_{L_\alpha}^{QS}C(k)\alpha_{3/4} \tag{40}$$

$$c_m = -\frac{c}{4V}\left(\pi\left(\frac{1}{2} - a\right)\dot{\theta} + \pi\frac{c}{2V}\left(\frac{1}{8} + a^2\right)\ddot{\theta} - a\pi\frac{\ddot{h}}{V}\right) + \frac{1}{2}c_{L_\alpha}^{QS}\left(\frac{1}{2} + a\right)C(k)\alpha_{3/4} \tag{41}$$

where a is defined in Figure 6. The function $C(k)$ is Theodorsen's function. The quasi-steady lift slope $c_{L_\alpha}^{QS}$ includes a compressibility correction using the Prandtl-Glauert factor.

The 2DOF section has two oscillatory modes: pitch and plunge. The structural frequencies of these modes vary with the appropriate stiffness and mass or inertia terms. As can be seen in Figure 5, the aerodynamic forces greatly depend on the frequency of the airfoil motion. In order to examine the aerodynamic damping at various frequencies, the stiffness terms, K_h and K_θ, were separately decreased from their original values
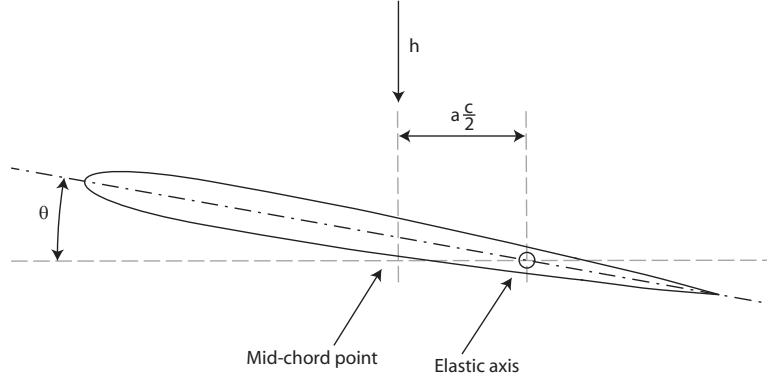
American Institute of Aeronautics and Astronautics

Figure 6: Schematic overview of airfoil

down to the point were the aeroelastic system becomes unstable. The resulting root locus plots are shown in Figure 7.
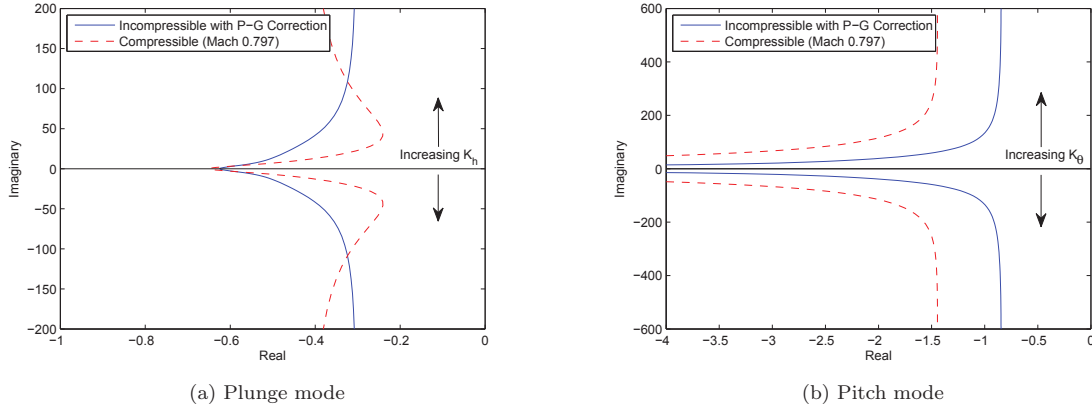

(a) Plunge mode

(b) Pitch mode

Figure 7: Root locus of oscillatory modes with varying stiffness for incompressible unsteady aerodynamics with Prandtl-Glauert correction and compressible aerodynamics at Mach 0.797

In Figure 7a, the aerodynamic damping of the plunge mode can be seen. At low frequencies the aerodynamic damping is much lower in the compressible case. As the frequency increases, the compressible aerodynamic damping increases and at high frequencies it exceeds the incompressible aerodynamic damping. The aerodynamic damping of the pitch mode is lower in the compressible case at all frequencies, as can be seen in Figure 7b. Overall the aerodynamic damping is larger in the compressible formulation, except for the plunge mode at low frequencies. This observation is not necessarily general for any plunge mode because of the intricate interaction between pitch and plunge motions.

V. VCCTEF Dynamics

A dynamic model governing the motion of the fast acting trailing edge flaps of the VCCTEF is developed and is coupled to the flight dynamic and aeroelastic model to establish an aeroservoelastic flight dynamic model.

American Institute of Aeronautics and Astronautics

A. Structural Dynamics

The dynamic model includes structural inertia and damping properties of the 16 control surfaces on each wing, as well as stiffness properties of the elastomer skin that is applied between the upper and lower surfaces of the flaps, as shown in Figure 3. Structural inertia and damping were estimated using data obtained from a model of the VCCTEF that is developed by Boeing.[23]

Stretching of the elastomer due to the relative deflection of adjacent flaps, $\Delta\delta$, makes it act as a nonlinear spring. The relative deflection is limited to magnitudes less than or equal to $2\,\mathrm{deg}$ in order to avoid the formation of drag inducing discontinuities and to prevent structural damage to the flap system. It can therefore be assumed that the stretching of the elastomer is limited to the linearly elastic domain and adheres to Hooke's Law

$$\epsilon = \frac{\sigma}{E} \tag{42}$$

where ϵ is the strain, σ is the tensile stress, and E is the elastic modulus of the elastomer, which is assumed to be constant. Furthermore, it is assumed that the shear stress carried by the thin elastomer skin is negligible.

The elastomer is installed under some tension σ_0 in order to prevent it from flapping if $\Delta\delta = 0$. The corresponding tensile force is given by

$$T_0 dx = \sigma_0 t dx \tag{43}$$

where t is the thickness of the elastomer skin and dx an infinitesimally narrow slice perpendicular to the chordwise coordinate x, as shown in Figure 8.
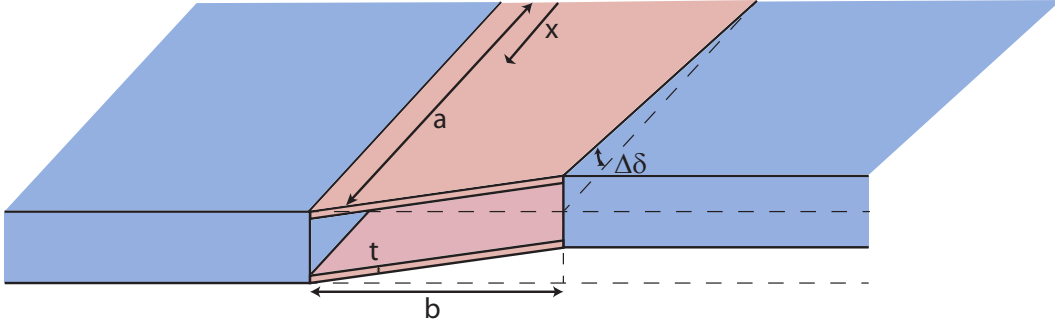

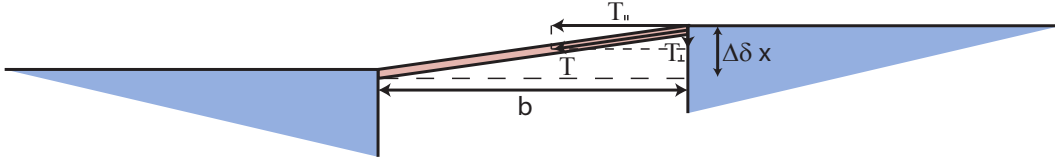Figure 8: Elastomer material between adjacent VCCTEF sections

Figure 9: Trailing edge view of upper elastomer material between adjacent VCCTEF sections

A relative deflection $\Delta\delta$, assumed small, leads to an additional elastomer strain $\Delta\epsilon$ given by

$$\Delta\epsilon\left(x\right) = \frac{\sqrt{\left(x\Delta\delta\right)^2 + b^2} - b}{b} = \frac{1}{b}\sqrt{\left(x\Delta\delta\right)^2 + b^2} - 1 \tag{44}$$

where b is the elastomer width and x indicates chordwise location. The resulting additional tensile force is given by

$$\Delta T\,\mathrm{d}x = tE\Delta\epsilon\left(x\right)\mathrm{d}x \tag{45}$$

and the total tensile force by

$$T\,\mathrm{d}x = \left(T_0 + \Delta T\right)\mathrm{d}x \tag{46}$$

Only the tensile force component perpendicular to the flap hinge line will contribute to the hinge moment. As shown in Figure 9, this component is given by

$$T_\perp \, \mathrm{d}x = \frac{x\Delta\delta}{\sqrt{(x\Delta\delta)^2 + b^2}} T \, \mathrm{d}x \tag{47}$$

The total hinge moment can now be found by integrating the product of the perpendicular tensile force component and its moment arm. The factor 2 is introduced to account for both the upper and lower elastomer material.

$$M = 2 \int_0^a x \frac{x\Delta\delta}{\sqrt{(x\Delta\delta)^2 + b^2}} \left(\sigma_0 t - tE + \frac{tE}{b} \sqrt{(x\Delta\delta)^2 + b^2} \right) \mathrm{d}x \tag{48}$$

$$= 2 \int_0^a (\sigma_0 t - tE) \, \Delta\delta \frac{x^2}{\sqrt{(x\Delta\delta)^2 + b^2}} dx + 2 \int_0^a \frac{tE}{b} x^2 \Delta\delta \, \mathrm{d}x \tag{49}$$

$$= 2 \frac{(\sigma_0 t - tE)}{2\Delta\delta^2} \left(a\Delta\delta\sqrt{(x\Delta\delta)^2 + b^2} - b^2 \log\left(a\Delta\delta + \sqrt{(x\Delta\delta)^2 + b^2} \right) - b^2 \log(b) \right) + 2\frac{tE}{3b} a^3 \Delta\delta \tag{50}$$

This nonlinear moment equation can be approximated using a Taylor series. The first three terms of this series are given by

$$M = \frac{2t\sigma_0 a^3}{3b}\Delta\delta - \frac{t(\sigma_0 - E)a^5}{5b^3}\Delta\delta^3 + \frac{3t(\sigma_0 - E)a^7}{28b^5}\Delta\delta^5 + \dots \tag{51}$$

It can be seen that the first term is linear in the pre-tension σ_0 and zero if $\sigma_0 = 0$. The geometric parameters a and b are a function of the flap lay-out and can be taken from Figure 3. The values of tE and $t\sigma_0$ were estimated by fitting the moment equation to notional data.[23] The resulting Taylor approximations of various orders can be seen in Figure 10 along with the analytical solution as given in equation (50). The data in the figure corresponds to the outer wing flaps. It can be observed that the third-order Taylor series is able to approximate equation (50) very well within the relevant domain $-2 \deg \leq \Delta\delta \leq 2 \deg$. It was therefore chosen to model the elastomer material as a torsion spring with linear and cubic terms.

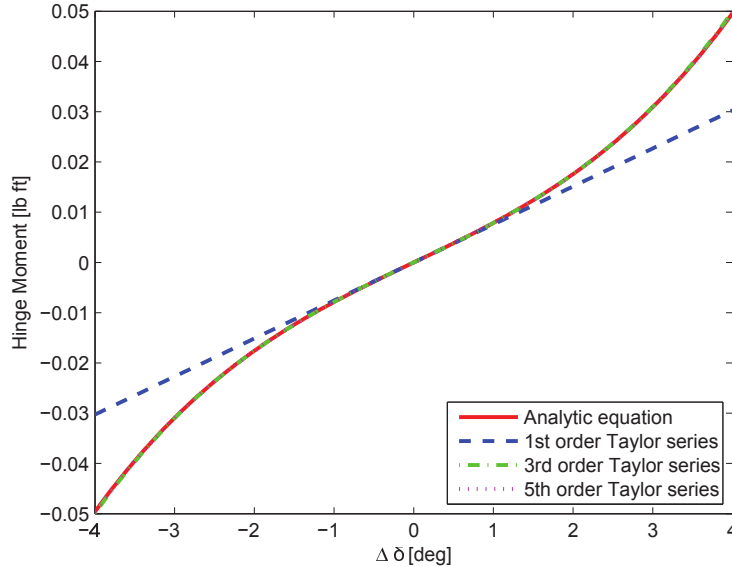Figure 10: Hinge moment due to elastomer stretching by nonzero relative deflection of adjacent VCCTEF segments

American Institute of Aeronautics and Astronautics

B. Aerodynamic Forces and Moments due to VCCTEF

The VCCTEF is attached to the flexible wing and hence creates aerodynamic forces and moments that can directly excite the elastic modes of the wing. The unsteady circulatory and noncirculatory forces and moments are time-dependent, like the unsteady aerodynamics of the elastic wing. Indicial function approximations for a flapped airfoil were developed by Hariharan and Leishman, using a combination of linear unsteady theory and aerodynamic reverse-flow theorems.[22] The corresponding aerodynamic lag states z_1 to z_{10} are numbered such that the notation of Hariharan and Leishman is maintained.[22] Again, quasi-steady vortex-lattice results are indicated by the superscript QS.

The sectional circulatory lift is given by

$$\dot{z}_1 = z_2 \tag{52}$$

$$\dot{z}_2 = -b_1^f b_2^f \left(\frac{2V}{c}\right)^2 \beta^4 z_1 - \left(b_1^f + b_2^f\right)\frac{2V}{c}\beta^2 z_2 + \delta_{qs} \tag{53}$$

and

$$c_L^{c,\delta} = c_{L_\delta}^{QS}\left(b_1^f b_2^f \left(\frac{2V}{c}\right)^2 \beta^4 z_1 + \left(a_1^f b_1^f + a_2^f b_2^f\right)\frac{2V}{c}\beta^2 z_2\right) \tag{54}$$

where $b_1^f = 0.366$, $b_2^f = 0.102$, $a_1^f = 0.918$, $a_2^f = 0.082$,[22] and

$$\delta_{qs} = \delta + \frac{1}{2}\frac{c}{2V}\frac{T_{11}}{T_{10}}\dot{\delta} \tag{55}$$

with the $T.$ geometric coefficients as defined in Appendix A, and δ and $\dot{\delta}$ the local flap deflection angle and deflection rate, respectively. Note that δ_{qs} is defined such that $c_L^{c,\delta} = c_{L_\delta}^{QS}\delta$ in case of a constant flap deflection. This definition differs somewhat from the one used by Hariharan and Leishman,[22] but the ratio of the δ and $\dot{\delta}$ contributions is maintained.

Dynamics of the sectional noncirculatory lift are represented by two aerodynamic lag states, as

$$\dot{z}_5 = -\frac{1}{K_{L_\delta}T_I}z_5 + \delta \tag{56}$$

$$\dot{z}_8 = -\frac{1}{K_{L_{\dot{\delta}}}T_I}z_8 + \frac{c}{V}\dot{\delta} \tag{57}$$

with the time constants K_{L_δ} and $K_{L_{\dot{\delta}}}$ as given in Appendix B. The noncirculatory lift is then given by

$$c_L^{nc,\delta} = \Delta c_{L_\delta}\dot{z}_5 + \Delta c_{L_{\dot{\delta}}}\dot{z}_8 \tag{58}$$

with Δc_{L_δ} and $\Delta c_{L_{\dot{\delta}}}$ as given in Appendix C. Equations (56), (57), and (58) are written in the same form as by Hariharan and Leishman.[22] It may seem as if the noncirculatory lift is a function of flap angle and angular speed, due to the formulation of equations (56) and (57) as a function of δ and $\dot{\delta}$. However, since $\dot{z}_5$ and $\dot{z}_8$ go to zero for constant values of respectively δ and $\dot{\delta}$, the noncirculatory lift is actually a function of flap angular speed and angular acceleration. This dependency is also present in the incompressible solution by Theodorsen[4] and can be made evident by differentiating equations (56) and (57) with regard to time:

$$\ddot{z}_5 = -\frac{1}{K_{L_\delta}T_I}\dot{z}_5 + \dot{\delta} \tag{59}$$

$$\ddot{z}_8 = -\frac{1}{K_{L_{\dot{\delta}}}T_I}\dot{z}_8 + \frac{c}{V}\ddot{\delta} \tag{60}$$

This can be rewritten using the substitutions $\bar{z}_5 = \dot{z}_5$ and $\bar{z}_8 = \dot{z}_8$, as

$$\dot{\bar{z}}_5 = -\frac{1}{K_{L_\delta}T_I}\bar{z}_5 + \dot{\delta} \tag{61}$$

$$\dot{\bar{z}}_8 = -\frac{1}{K_{L_{\dot{\delta}}}T_I}\bar{z}_8 + \frac{c}{V}\ddot{\delta} \tag{62}$$

The noncirculatory lift is then given by

$$c_L^{nc,\delta} = \Delta c_{L_\delta} \bar{z}_5 + \Delta c_{L_{\dot\delta}} \bar{z}_8 \tag{63}$$

Similar reformulations can also be done for subsequent expressions of the same form for the noncirculatory pitching and hinge moments.

The circulatory moment about the elastic axis location is given by

$$\dot{z}_3 = -\frac{2V}{c} b_3^f \beta^2 z_3 + \delta_{qs_m} \tag{64}$$

and

$$c_m^{c,\delta} = c_{m_\delta}^{QS} \frac{2V}{c} b_3^f \beta^2 z_3 \tag{65}$$

where $b_3^f = 1.5$ as given by Hariharan and Leishman,[22] and

$$\delta_{qs_m} = \delta + \frac{2T_1 - 2T_8 - (2f+1)T_4 + T_{11}}{2T_4 + 2T_{10}} \frac{c}{2V} \dot\delta \tag{66}$$

with f as defined in Figure 11. The definition of δ_{qs_m} differs somewhat from the one used by Hariharan and Leishman,[22] but the ratio of the δ and $\dot\delta$ contributions is maintained. Since the quasi-steady moment coefficient $c_{m_\delta}^{QS}$ corresponds to the moment about the elastic axis location, a translation, such as given by equation (36), is not necessary. It is assumed that the transient behavior of the circulatory moment about the elastic axis location is proportional to that of the circulatory moment about the quarter chord point.
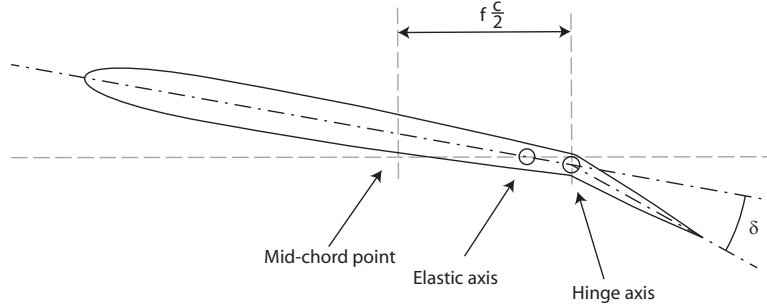

Figure 11: Schematic overview of airfoil with flap

The time-dependent behavior of the noncirculatory moment about the quarter chord point is modeled by two aerodynamic lag states,[22] as

$$\dot{z}_6 = -\frac{1}{K_{m_\delta} T_I} z_6 + \delta \tag{67}$$

$$\dot{z}_9 = -\frac{1}{K_{m_{\dot\delta}} T_I} z_9 + \frac{c}{V} \dot\delta \tag{68}$$

with the time constants K_{m_δ} and $K_{m_{\dot\delta}}$ as given in Appendix B. The corresponding output equation is

$$c_m^{nc,\delta}{}_l = \Delta c_{m_\delta} \dot{z}_6 + \Delta c_{m_{\dot\delta}} \dot{z}_9 \tag{69}$$

with Δc_{m_δ} and $\Delta c_{m_{\dot\delta}}$ as given in Appendix C. The noncirculatory moment about the elastic axis can be calculated analogous to the manner shown in equation (37).

American Institute of Aeronautics and Astronautics

C. Aerodynamic Hinge Moment due to Rigid Body and Elastic Wing

The aerodynamic hinge moment due to rigid body and elastic wing involves integration of the pressure distribution on the flap. However, reverse-flow theorems apply only to total forces and moments on the airfoil.[22] Instead, the incompressible circulatory hinge moment coefficient as derived by Theodorsen[4] was corrected using the Prandt-Glauert factor in order to model the hinge moment due to the rigid body and elastic wing. The rigid-body contribution is assumed quasi-steady. For the elastic wing contribution it was assumed that the transient behavior is proportional to that of the unsteady circulatory lift and moment. The circulatory hinge moment coefficient due to the elastic wing is thus given by

$$c_h^e = -\frac{1}{2}\frac{T_{12}}{\beta}\frac{2V}{c}\beta^2 \left(a_1 b_1 x_1 + a_2 b_2 x_2\right) \tag{70}$$

with x_1 and x_2 as given in equations (8) and (9), respectively.

D. Aerodynamic Hinge Moment due to VCCTEF

The aerodynamic hinge moment due to VCCTEF is the self-induced hinge moment due to the flap deflection and deflection rate. It includes circulatory and noncirculatory contributions. Hariharan and Leishman[22] assume that the hinge moment is equal to the total moment on the airfoil at the instant of the flap deflection in order to be able to utilize results from reverse-flow theorems.

The circulatory hinge moment due to flap deflection is given by Hariharan and Leishman[22] as

$$\dot{z}_4 = -\frac{2V}{c}b_3^f\beta^2 z_4 + \delta_{qs_h} \tag{71}$$

and its corresponding output equation

$$c_h^{c,\delta} = c_{h_\delta}^{QS}\frac{2V}{c}b_3^f\beta^2 z_4 \tag{72}$$

where

$$\delta_{qs_h} = \delta + \frac{T_{11}\left(T_{12} - 2T_4\right)}{T_5 - T_4 T_{10} + T_{12}T_{10}}\frac{c}{2V}\dot{\delta} \tag{73}$$

The definition of δ_{qs_m} is adapted such that the ratio of the δ and $\dot{\delta}$ contributions is maintained.

The time-dependent behavior of the noncirculatory hinge moment is modeled by two aerodynamic lag states,[22] as

$$\dot{z}_7 = -\frac{1}{K_{h_\delta}T_I}z_7 + \delta \tag{74}$$

$$\dot{z}_{10} = -\frac{1}{K_{h_\delta}T_I}z_{10} + \frac{c}{V}\dot{\delta} \tag{75}$$

with the time constants K_{h_δ} and $K_{h_{\dot{\delta}}}$ as given in Appendix B. The corresponding output equation is

$$c_h^{nc,\delta} = \Delta c_{h_\delta}\dot{z}_7 + \Delta c_{h_{\dot{\delta}}}\dot{z}_{10} \tag{76}$$

with Δc_{h_δ} and $\Delta c_{h_{\dot{\delta}}}$ as given by in Appendix C.

E. Actuator Model

A direct current electric torque motor model forms the basis of the actuator model:

$$L\dot{M}^m + RM^m = \left(V - V_b\right)K_m \tag{77}$$

$$V_b = K_b\dot{\delta} \tag{78}$$

where M^m is the electric torque motor hinge moment, V is the input voltage, V_b is the back voltage, K_m is the torque to current ratio, K_b is the back EMF constant, L is the inductance, and R is the resistance. The input voltage is set using a PID-controller with the commanded flap deflection as its input:

$$V = K_P\left(\delta_c - \delta\right) + K_I\int\left(\delta_c - \delta\right)\mathrm{dt} - K_D\dot{\delta} \tag{79}$$

American Institute of Aeronautics and Astronautics

VI. Turbulence Model

For the purpose of simulation of the flight dynamic and aeroelastic response to atmospheric disturbances, a turbulence model was devised. The model is also relevant for the design and evaluation of flight control laws that include gust load alleviation and flutter suppression.

A.   2D Von Karman Turbulence Generation

For simulations of atmospheric flight dynamics of rigid-body vehicles, turbulence models that include velocity components as well as rotational rates are often used. Examples include the linear field approximation and Etkin's four-point model.[24] While these models include information on the local turbulence velocity and its spatial gradients, a complete spatial turbulence description is not included.

The aeroelastic response of an aircraft is strongly dependent on the lift distribution and therefore on the local angle of attack along the wing. The angle of attack in turn is a function of the local turbulence velocity. Therefore a spatial turbulence description that varies longitudinally and laterally is necessary to obtain a realistic aeroelastic response of the aircraft. The spatial dependence of the turbulence is illustrated in Figure 12.

(a) 1D Von Karman Turbulence Field   (b) 2D Von Karman Turbulence Field
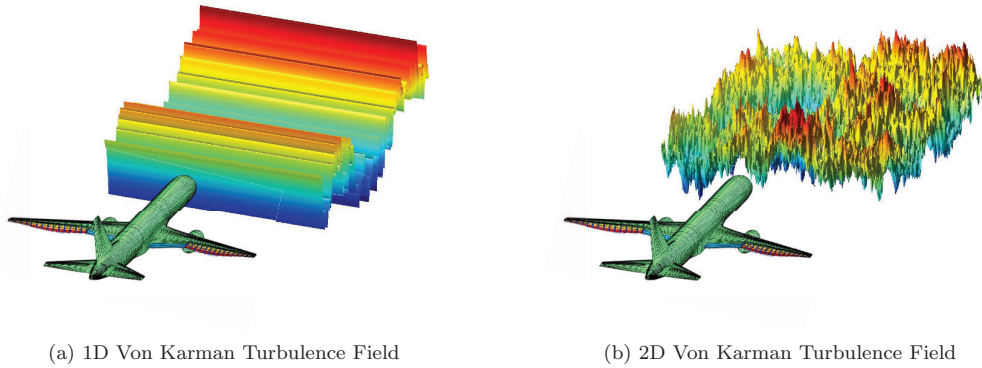
Figure 12: Illustration of 1D and 2D Turbulence

In order to simplify the turbulence description, several assumptions are made. The turbulence is assumed to be a homogeneous, stationary, and Gaussian random process. Furthermore, only vertical turbulence speed is considered, since it has the strongest effect on the twist, flapwise bending, and vertical displacement of the wing. Together with the assumption that the vertical component of the flight path is negligible, this leads to a two-dimensional isentropic turbulence field. Consequently, the turbulence is also ergodic. A final assumption is made by neglecting the evolution of the turbulence field as a function of time, thus seeing it as a spatial field that is frozen in time. This is known as Taylor's frozen field hypothesis.[25]

Within this framework of assumptions different turbulence models, defined by their correlation or spectra functions, can be utilized. Two of the most common ones being the Dryden and Von Karman spectra. For high frequencies the Von Karman spectrum has a roll-off proportional to $\Omega^{-\frac{5}{3}}$, where Ω is the spatial frequency, satisfying the Kolmogorov law.[26] Its spectral power at high frequencies exceeds the Dryden spectrum, which has a roll-off proportional to Ω^{-2}. The larger presence of high frequency turbulence in the Von Karman model increases its realism.[27] This is especially relevant for simulations of aeroelastic phenomena, which generally occur at higher frequencies than flight dynamic responses.

The most widespread method to obtain one-dimensional turbulence signals is filtering of a white noise signal. One of the advantages of one-dimensional Dryden turbulence is the fact that it is based on a rational spectrum and can thus be generated using a difference equation that can easily be obtained from the spectrum or correlation function. Von Karman turbulence, on the other hand, is described by an irrational spectrum and thus requires an approximate difference equation. While various approximations of different orders exist, a high-order approximation is required to be able to correctly represent high-frequency spectral content.[28] For the current application of generating two-dimensional turbulence fields, this disadvantage of the Von

Karman turbulence spectrum is however not relevant, since it is not possible to obtain difference equations for multi-dimensional functions of inseparable variables. For the current study the Von Karman spectrum was selected.

For generation of the two-dimensional turbulence field, a method based on convolution or the Fourier transform has to be used. In this case the latter is selected. The method, based on existing work,[26,27] is outlined below.

The Von Karman energy spectrum function is given by

$$E(\nu) = \frac{110}{9}\sigma^2 L \frac{(2\pi aL\nu)^4}{\left[1 + (2\pi aL\nu)^2\right]^{17/6}} \tag{80}$$

where $\nu = \left(\nu_1^2 + \nu_2^2 + \nu_3^2\right)^{1/2}$ is the norm of the spatial frequency components, a is a constant equal to 1.339, σ^2 is the turbulence variance, and L is its length scale. The corresponding autospectrum is given by

$$\Phi_{ii}(\nu_1, \nu_2, \nu_3) = \frac{440\pi^3}{9} \frac{\sigma^2 a^4 L^5 \left(\nu^2 - \nu_i^2\right)}{\left[1 + (2\pi aL\nu)^2\right]^{17/6}} \tag{81}$$

The two-dimensional spectra can now be obtained by the integral

$$\Psi_{ij}(\nu_1, \nu_2) = \int\limits_{-\infty}^{\infty} \Phi_{ij}(\nu_1, \nu_2, \nu_3)\,\mathrm{d}\nu_3 \tag{82}$$

The resulting two-dimensional vertical turbulence spectrum is

$$\Psi_{33}(\nu_1, \nu_2) = \frac{64\pi^3}{9}\sigma^2 (aL)^4 \frac{\nu_1^2 + \nu_2^2}{\left[1 + (2\pi aL)^2 (\nu_1^2 + \nu_2^2)\right]^{7/3}} \tag{83}$$

In order to obtain the turbulence field corresponding to equation (83), Gaussian white noise is multiplied with the relevant shaping function in the frequency domain and subsequently transformed to the spatial domain using the two-dimensional Inverse Fast Fourier Transform (IFFT). Gaussian white noise can be generated in the spatial domain and transformed to the frequency domain using the two-dimensional Fast Fourier Transform (FFT). However, in order to reduce computational effort it can also be generated directly in the frequency domain, using the Hermitian symmetry properties of the FFT of a real-valued signal.[27]

The spectral density of the output signal of a linear filter is given by

$$\Phi_w(\nu) = |H(\nu)|^2 \Phi_n(\nu) \tag{84}$$

where $H(\nu)$ is the frequency response function of the filter, $\Phi_w(\nu)$ is the desired turbulence spectrum, as given by equation (83). If $\Phi_n(\nu)$ is the spectrum of Gaussian white noise with unity variance, the solution for the frequency response function of the required filter is given by

$$H(\nu_1, \nu_2) = \sqrt{\nu_{s1}\nu_{s2}\Psi_{33}(\nu_1, \nu_2)}e^{j\alpha(\nu_1, \nu_2)} \tag{85}$$

where $\alpha(\nu_1, \nu_2)$ is an arbitrary phase function, which can be set to zero. Note the correction due to the effect of the sampling frequency of the white noise with unity variance.

The spatial sampling frequencies are set using the aircraft speed and time step in the longitudinal direction, and using the strip theory discretization in the lateral direction:

$$\nu_{s1} = \frac{1}{V\Delta t} \tag{86}$$

$$\nu_{s2} = \frac{1}{\Delta y} \tag{87}$$

After frequency domain multiplication and subsequent IFFT a spatial turbulence field is obtained. Vertical speeds at the required positions are obtained using cubic interpolation. An example of a Von Karman realization is shown in Figure 13.
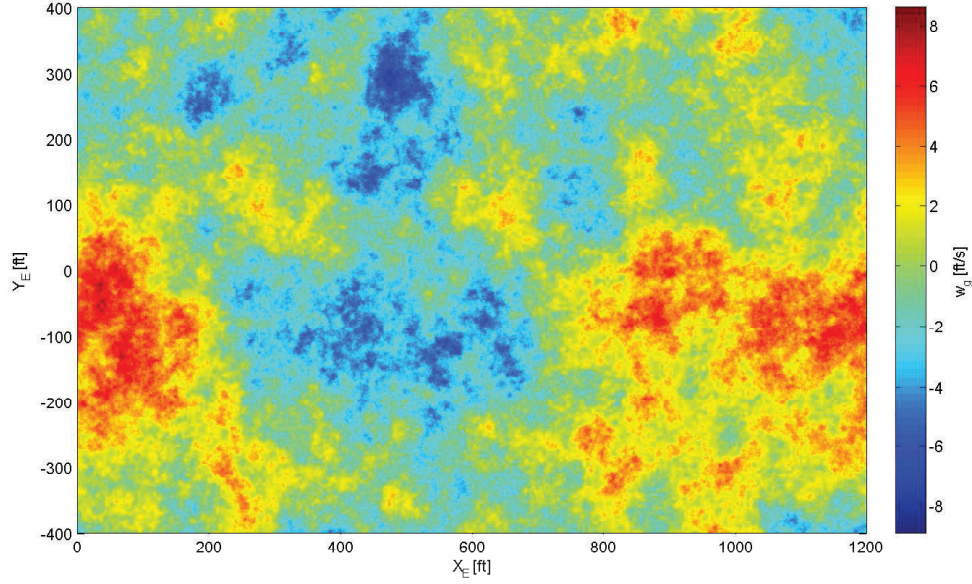
American Institute of Aeronautics and Astronautics

Figure 13: Von Karman vertical turbulence field with $L = 2500$ ft and $\sigma = 4.7$ ft/s

B. Gust Field Generation

In addition to stochastic turbulence from the Von Karman turbulence model, deterministic gust fields can also be useful for evaluation of flight performance and controller design. Consecutive $1 - \cos$ gusts at preselected frequency and specific location can be used to excite particular flight dynamic or aeroelastic modes. A high-frequency gust field below the wing can for example be used to excite aeroelastic bending modes as will be shown later. Other available gust fields include the sharp-edged gust and the canyon gust, which has a sharp increase and decreases linearly.

C. Aerodynamic Forces and Moments due to Turbulence and Gusts

The turbulence and gust field expressions described above can be used to determine the local vertical turbulence speed at locations on the rigid fuselage and horizontal tail plane, and on the elastic wing. The aerodynamic forces and moments due to the vertical turbulence are subject to time-dependent effects. In case of incompressible flow, the indicial lift function of an airfoil penetrating a sharp-edged gust is given by Küssner's unsteady gust response function.[29] For practical purposes, Küssner's function is often approximated[15] as

$$\psi_g(S) = 1 - 0.5e^{-0.130S} - 0.5e^{-S} \tag{88}$$

Similar indicial functions for subsonic flow are given by Leishman.[30] Functions based on both linear theory and CFD are given. For the current study, the following function, based on linear theory, is used:

$$\psi_g(S, M) = 1 - G_1 e^{-g_1 \beta^2 S} - G_2 e^{-g_2 \beta^2 S} = 1 - 0.527 e^{-0.100 \beta^2 S} - 0.473 e^{-1.367 \beta^2 S} \tag{89}$$

The difference between equations (88) and (89) can clearly be observed in Figure 14. The indicial response in compressible flow is decreased relative to Küssner's function. Hence calculation of gust loads based on Küssner's function may lead to overestimation of such loads, but is conservative for design purposes.

By virtue of Duhamel's integral, the compressible indicial function can be applied to a random gust input
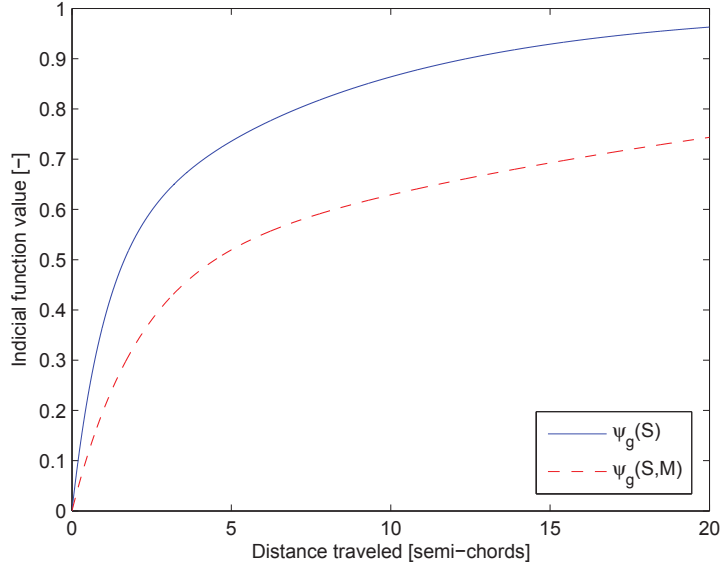
American Institute of Aeronautics and Astronautics

Figure 14: Comparison of Küssner's gust response function and a compressible gust response function at $M = 0.797$

using a state-space realization with

$$\dot{x}_1^g = x_2^g \tag{90}$$

$$\dot{x}_2^g = -g_1 g_2 \left(\frac{2V}{c}\right)^2 \beta^4 x_1^g - (g_1 + g_2) \left(\frac{2V}{c}\right) \beta^2 x_2^g + \frac{w_g}{V} \tag{91}$$

and the output equation

$$\alpha_g = g_1 g_2 \left(\frac{2V}{c}\right)^2 \beta^4 x_1^g + (G_1 g_1 + G_2 g_2) \left(\frac{2V}{c}\right) \beta^2 x_2^g \tag{92}$$

with α_g the local effective angle of attack due to the vertical gust.

The circulatory lift and moment contributions towards the rigid-body flight dynamics, elastic wing dynamics and VCCTEF flap dynamics are calculated using α_g and the their steady-state values, as described in preceding sections. It should be noted that w_g in equation (91) corresponds to the vertical gust speed at the section leading edge. A transport delay must thus be applied to account for planform geometry. Ensuing gust penetration at the leading edge, the point at which lift acts quickly moves aft.[15] It is therefore assumed that the lift acts at its steady-state location throughout the maneuver.

VII. Flight Dynamic and Aeroservoelastic Coupling

The aerodynamic coefficients C_L, C_D, C_y, C_l, C_m, and C_n are a function of the aeroelastic deflections of the aircraft wings as shown in Section IV. Therefore, the flight dynamic equations of motion of the aircraft are coupled with the aeroelastic equations via the aerodynamic coefficients. The aeroelastic modes can be decomposed into symmetric and antisymmetric motions. The lift, drag, and pitching moment coefficients are influenced by symmetric aeroelastic modes, while the side force, rolling moment, and yawing moment coefficients are influenced by antisymmetric aeroelastic modes.[7]

The contributions of the unsteady elastic wing, VCCTEF, and gust aerodynamics to the rigid-body aerodynamic coefficients can be calculated by summing the contributions of the individual discretized wing strips, control surfaces, and individual discretized wing, fuselage and horizontal tail strips, respectively. The

American Institute of Aeronautics and Astronautics

effect of rigid-body motion on the elastic wing and VCCTEF is modeled through the notion of the local aeroelastic angle of attack, as mentioned above. In order to facilitate the coupling, the aeroservoelastic system is expressed by a state-space equation with rigid-body motion and orientation as inputs and aerodynamic coefficient contributions as outputs. The precise form of the state-space equations has been set forth in previous work.[7, 12] The aeroservoelastic output equation is given by

$$C_a^e = C_e \begin{bmatrix} x_e \\ \dot{x}_e \end{bmatrix} + C_x \begin{bmatrix} x_l \\ \dot{x}_l \end{bmatrix} + C_z \begin{bmatrix} z_l \\ \dot{z}_l \end{bmatrix} + C_g \begin{bmatrix} x_l^g \end{bmatrix} \tag{93}$$

where C_a^e is the aeroservoelastic contribution to the rigid-body aerodynamic coefficients, x_e is a vector containing the aeroelastic modal states, x_l is a vector containing all aerodynamic lag states corresponding to the aeroelastic behavior of the wing, z_l is a vector containing all aerodynamic lag states corresponding to the VCCTEF segments, and x_l^g is a vector containing all aerodynamic lag states corresponding to the unsteady turbulence. The output matrices C_e, C_x, C_z, and C_g are formulated such that the multiplication results in the total aerodynamic contributions of the aforementioned states.

The presence of the first term of equation (93) is solely due to the noncirculatory pitching moment due to angle of attack. As shown in equation (25), this pitching moment depends directly on the local angle of attack and thereby on the generalized displacement of the wing. All other unsteady aerodynamic forces and moments depend only on the aerodynamic lag states or their derivatives.

Since the linear aeroservoelastic system is coupled to a nonlinear flight dynamic model, it is possible to account for quadratic drag due to aeroelastic behavior. In order to do so, it is assumed that the drag coefficient can be estimated accurately via a drag polar model. The drag polar parameter is derived for each discretized strip using the local lift and drag coefficients. The result is a diagonal matrix containing the drag polar parameter of each strip. Using this matrix and the circulatory lift contribution of each strip, a quadratic induced drag term can be calculated and added to the rigid-body drag coefficient. The corresponding quadratic equation is given by

$$C_D^{xx} = x_l^T C_{xx} x_l + z_l^T C_{zz} z_l \tag{94}$$

where C_D^{xx} is the quadratic drag contribution, and C_{xx} and C_{zz} are the corresponding output matrices for the aeroelastic and VCCTEF aerodynamic lag state vectors, respectively.

The rigid-body flight dynamics are then given by

$$\dot{x}_r = f\left(x_r, \dot{x}_r, C_a^e, C_D^{xx}\right) \tag{95}$$

where f is a function containing the kinematic, dynamic, and aerodynamic equations for the aircraft in aeroelastic trim state.

VIII.   Simulation

Numerical simulations were performed using a nonlinear 6DOF flight dynamic model coupled with the full-order linear aeroelastic model. All simulations were initialized in steady symmetric straight level flight at 36,000 ft altitude and Mach 0.797.

A.   Numerical Integration

Simulations are performed using the full-order system. The coupled system contains both highly damped poles due to the aerodynamic lag states and aeroelastic modes at very high frequencies (up to the order of 10^4 rad/s).

The stiffness that is introduced into the system of differential equations by the aerodynamic lag states can lead to numerical instability in some, most notably explicit, integration methods. Therefore care must be taken in selecting the time step in case a conditionally stable time integration scheme is used.

On the other hand, some integration methods, such as the implicit Euler method, introduce numerical damping, which can lead to numerical stabilization of unstable modes. In order to address both of these potential issues, Newmark-β[31] was selected the as integration method.

By selecting coefficients $\beta = 0.25$ and $\gamma = 0.5$, the method has a stability region that coincides with the left half plane, and is $\mathcal{O}\left(\Delta t^2\right)$ accurate. In cases where unconditional stability is not required, e.g. for

American Institute of Aeronautics and Astronautics

simulation of a reduced order model with only poles at limited frequency, higher accuracy can be obtained by selecting different coefficients.

The coupled system consists of linear second-order differential equations for the elastic wing, linear first-order differential equations for the aerodynamic lag states, and nonlinear first-order differential equations for the aircraft dynamics and kinematics. The linear system is integrated using a hybrid scheme that combines the Newmark-β method for second-order equations with a second-order multi-step method for the linear first-order equations. In case $\beta = 0.25$ and $\gamma = 0.5$ are selected, this scheme is equivalent to the trapezoidal rule with constant acceleration for the second-order equations and constant speed for the first-order equations. The nonlinear differential equations are integrated using the fourth-order Runge-Kutta scheme.

B. Comparison with Incompressible Results

Figure 15 and 16 show the pitch rate and roll rate responses of the ESAC to symmetric and antisymmetric VCCTEF inputs, respectively. In both figures the incompressible response curve corresponds to a model of the ESAC where unsteady aerodynamics for compressible flow are not taken into account in the modeling of the time-dependent aerodynamic effects. Instead, it is based on the incompressible expressions as given by Theodorsen[4] with steady-state values corrected using the Prandtl-Glauert compressibility correction.

The oscillatory rigid-body modes and the first four elastic modes are indicated in the figures. The corresponding mode shapes are shown in Figure 17. Several differences can be observed in the frequency responses of the incompressible and compressible models. In the symmetric case the first mode is damped less in the compressible case, while elastic modes at higher frequencies are more damped. In the antisymmetric case the damping of the first mode is similar for both approximations, while the higher frequencies are more damped in the compressible case.

The first symmetric and antisymmetric modes are both bending modes. The fact that these low frequency bending modes have relatively low damping in the compressible case corresponds well to the observations that were made regarding Figure 7.
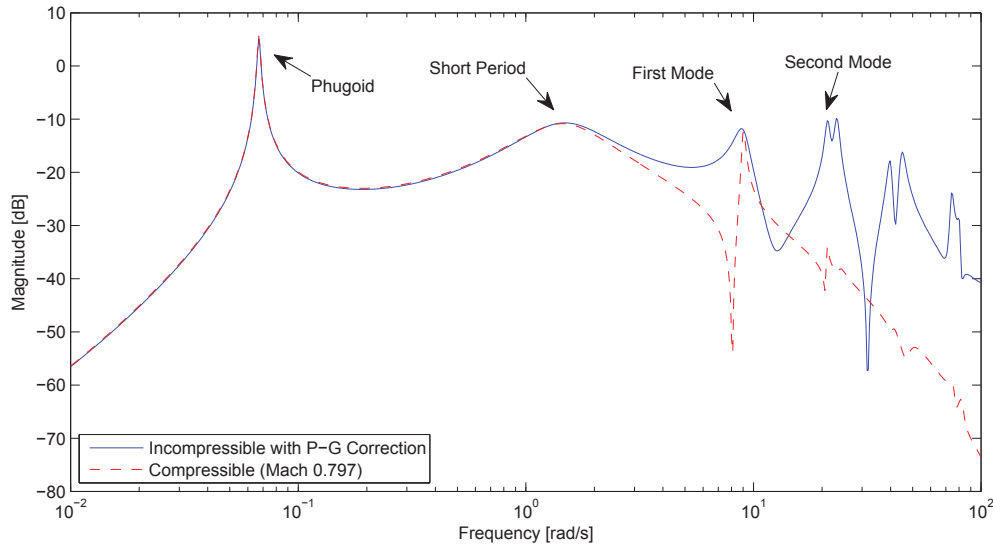

Figure 15: Pitch rate frequency response of ESAC to a symmetric semi-sinusoidally shaped VCCTEF input for incompressible and compressible unsteady aerodynamics approximations

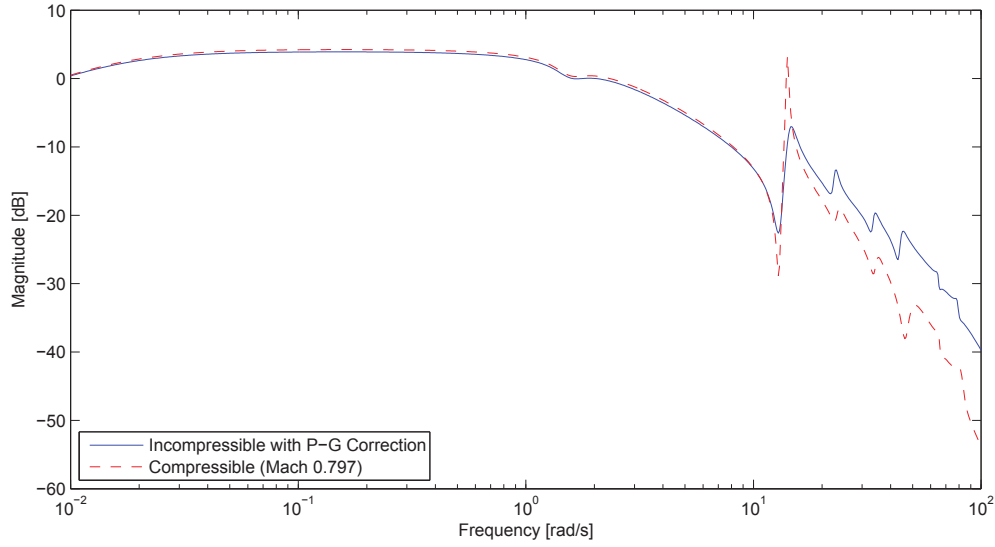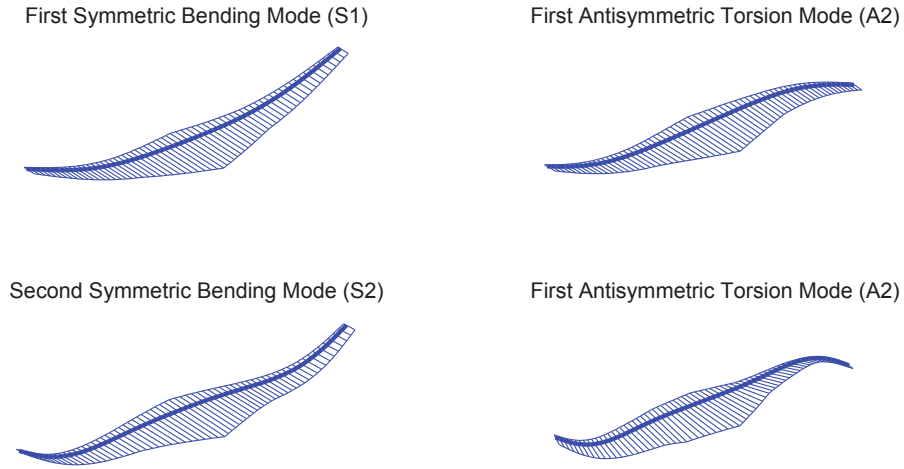American Institute of Aeronautics and Astronautics

Figure 16: Roll rate frequency response of ESAC to an antisymmetric semi-sinusoidally shaped VCCTEF input for incompressible and compressible unsteady aerodynamics approximations

Figure 17: Modes shapes of the first four elastic wing deformation modes

C.   Flight Dynamic Maneuver

Figures 19, 20, and 21 show flight dynamic, elastic wing, and aerodynamic hinge moment responses to a 2 deg antisymmetric VCCTEF doublet of semi-sinusoid shape as shown in Figure 18. The doublet commences at $t = 1$ s and changes sign at $t = 1.5$ s, $t = 2$ s, and $t = 3$ s. At $t = 4$ s the VCCTEF is set to zero deflection.

Figure 20 shows the response of the first four elastic wing deformation modes. The mode shapes corresponding to these modes are shown in Figure 17. Especially the first antisymmetric mode is excited, since the doublet is an antisymmetric input. In comparison to an unsteady aeroelastic model of the ESAC that

American Institute of Aeronautics and Astronautics

is based on incompressible with Prandtl-Glauert compressibility correction, the damping of the this elastic mode is quite low. Consequently, oscillations are sustained well after the VCCTEF is returned to zero deflection at $t = 4$ s. This highlights the need for closed-loop aeroelastic control for flexible vehicles, such as the ESAC.

As mentioned above, these results were obtained using Newmark-β integration for the aeroservoelastic system. The contrast with integration methods that add numerical damping, such as the implicit Euler method, is obvious in simulation of lightly damped modes. In a simulation of the same flight dynamic maneuver using the implicit Euler method, even the oscillations of the first antisymmetric mode were largely damped out within several seconds, as can be seen in Figure 22.

As expected, peaks occur in the aerodynamic hinge moment curve at points where the VCCTEF deflection is changed. This is due to unsteady hinge moment effects induced by the movement of the flap itself. After the doublet is finished, oscillatory behavior is still present in the hinge moment curve due to the sustained excitation of the aforementioned elastic wing mode.
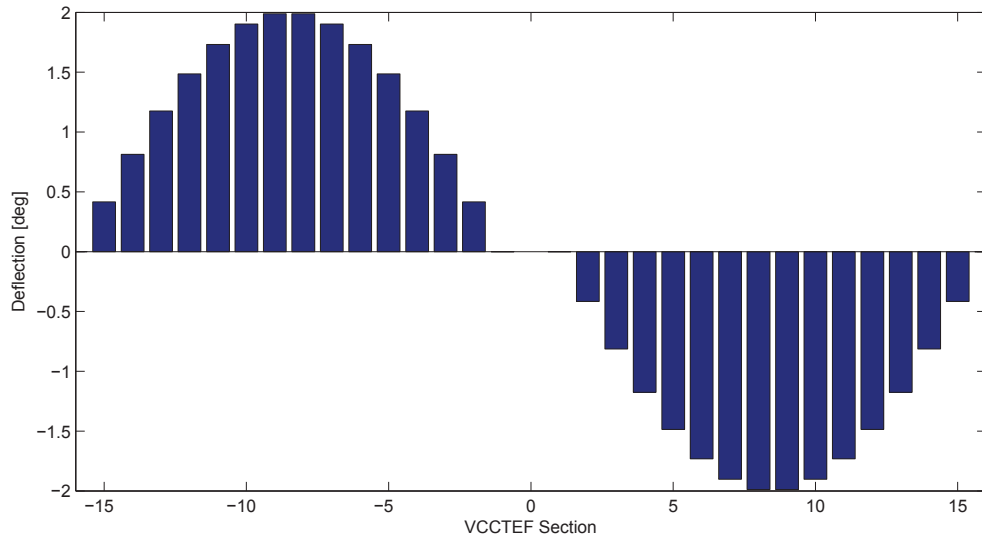
Figure 18: VCCTEF 2 deg antisymmetric semi-sinusoid doublet
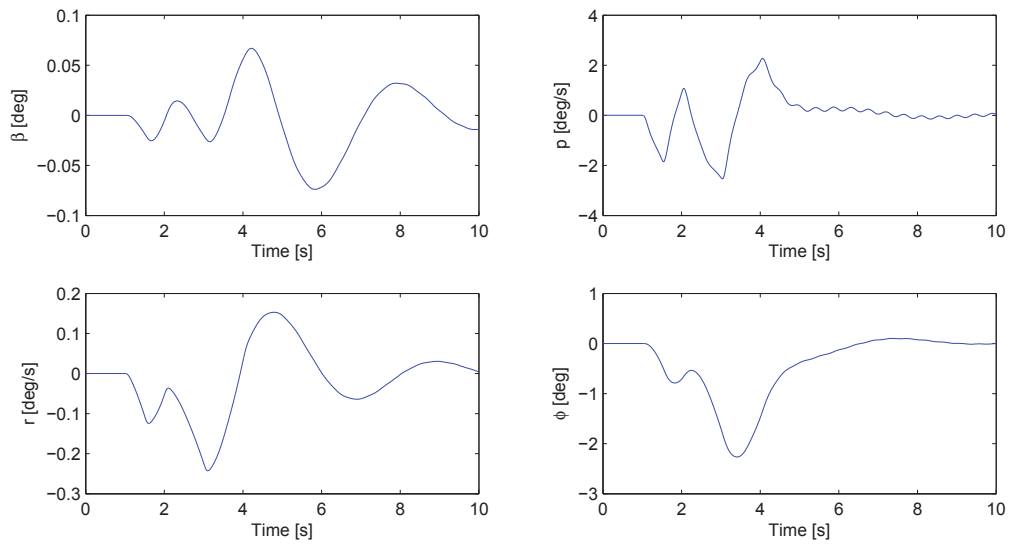
American Institute of Aeronautics and Astronautics

Figure 19: Flight dynamic response to antisymmetric VCCTEF doublet
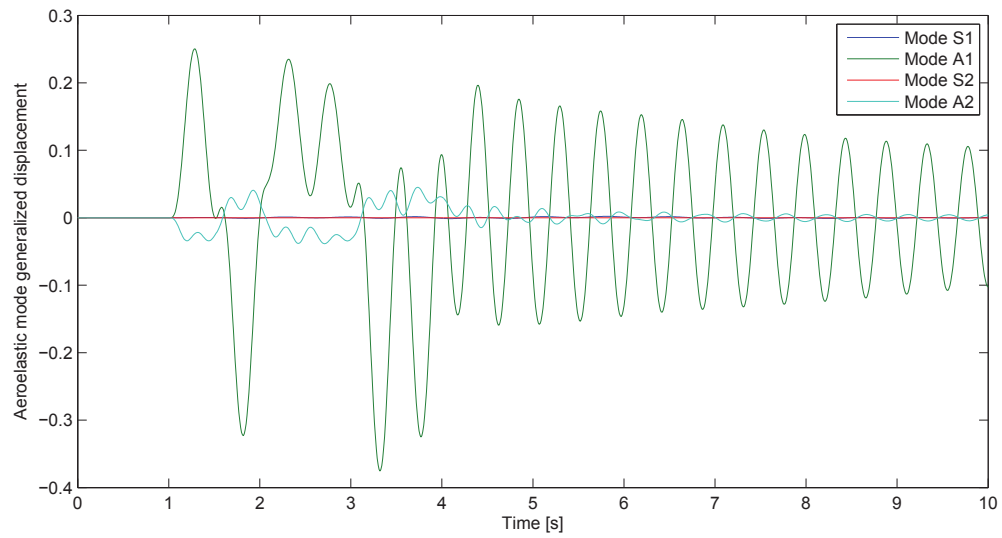

Figure 20: Elastic wing response showing displacement of first four elastic modes due to antisymmetric VCCTEF doublet
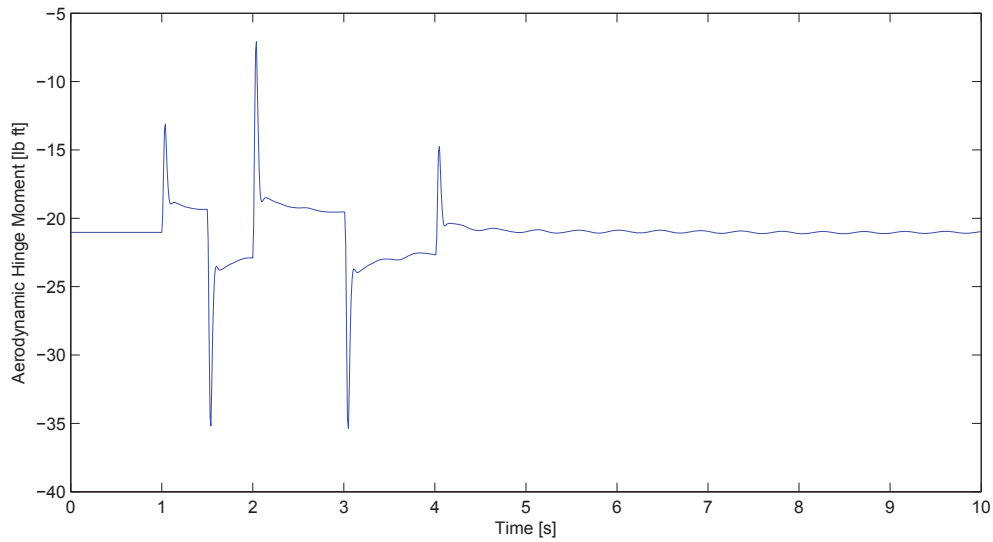
Figure 21: Aerodynamic hinge moment response of flap 5 on left wing to antisymmetric VCCTEF doublet
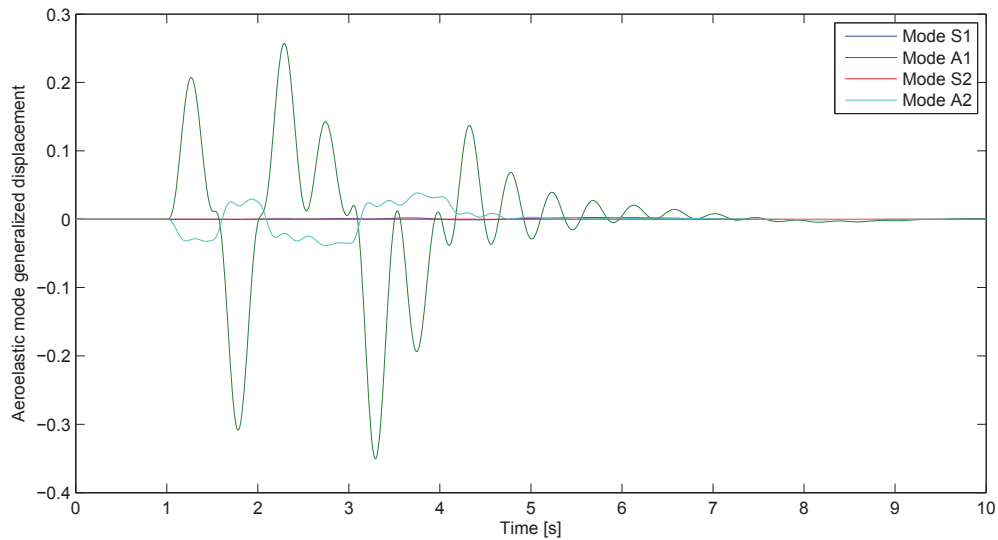

Figure 22: Elastic wing response showing displacement of first four elastic modes due to antisymmetric VCCTEF doublet using implicit Euler integration for the aeroservoelastic system

D. Von Karman Turbulence Response

Figures 23, 24, and 25 show flight dynamic, elastic wing, and aerodynamic hinge moment responses to a Von Karman vertical turbulence field. The turbulence field has standard deviation 4.7 ft/s and scale length 2500 ft. As such it can be classified as moderate turbulence.

Looking at Figure 23 it can be seen that the 2D turbulence field affects both longitudinal and lateral dynamics.

The turbulence is switched on at $t = 0$ s and is switched off at $t = 8$ s. The second point is well visible in the elastic response shown in Figure 24. Prior to $t = 8$ s the wing is in forced excitation and its response

American Institute of Aeronautics and Astronautics

seems random. After the turbulence field is switched off, the lightly damped first symmetric mode maintains oscillation at its natural frequency. Its coupling to the rigid-body dynamics can be observed in the pitch rate and also in the hinge moment shown in Figure 25.
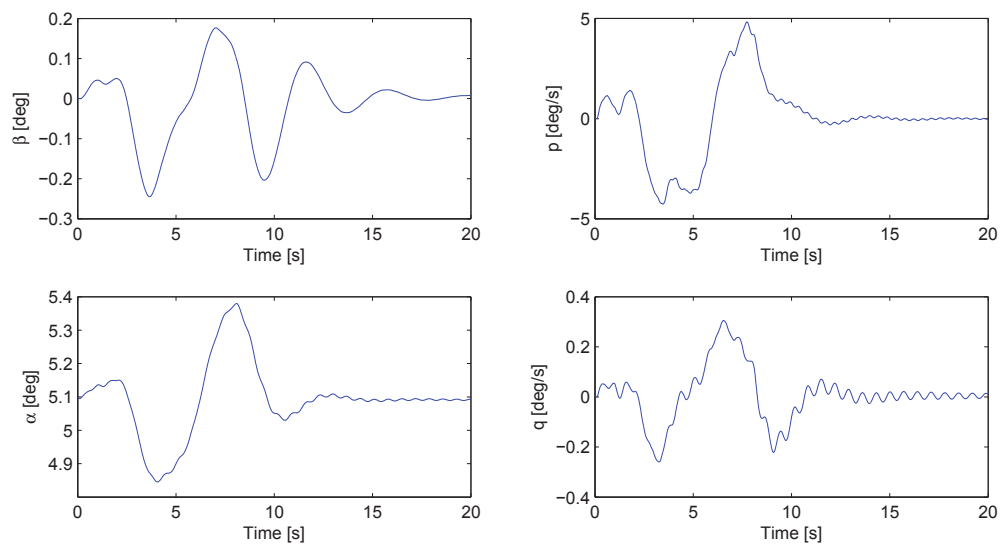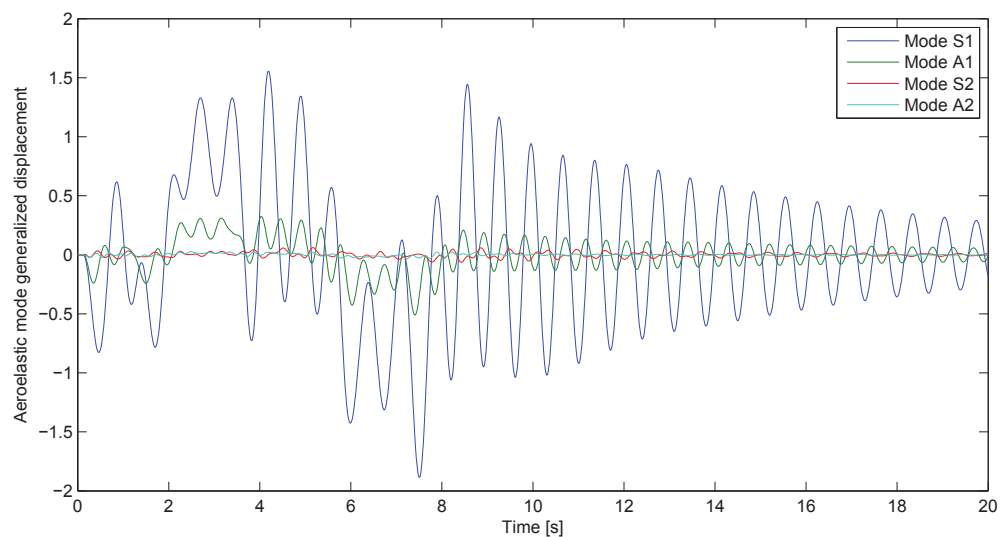

Figure 23: Flight dynamic gust response

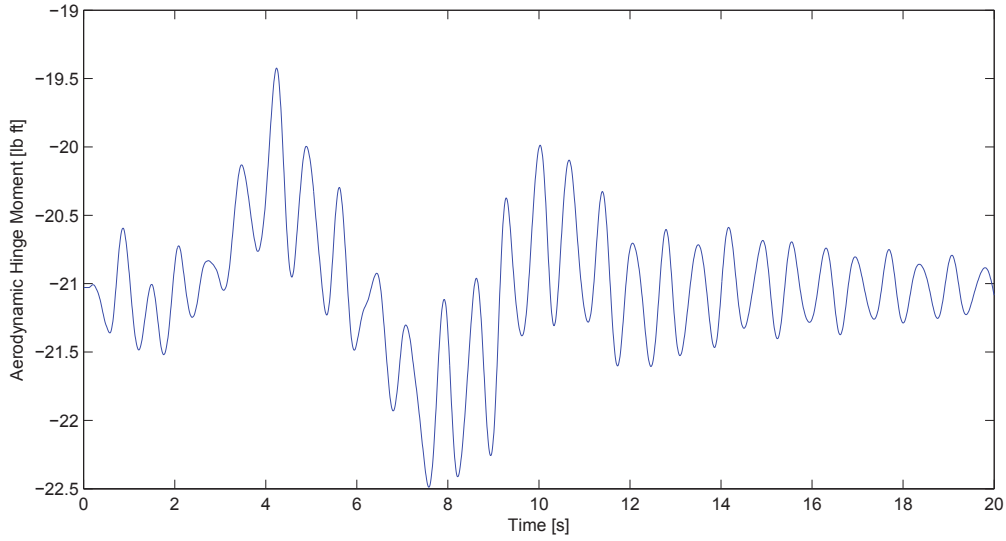Figure 24: Elastic wing gust response showing the displacement of the first four elastic modes

American Institute of Aeronautics and Astronautics

Figure 25: Aerodynamic hinge moment response of flap 5 on left wing

E. High Frequency Gust Response

Figures 26, 27, and 28 show flight dynamic, elastic wing, and aerodynamic hinge moment responses to a series of $1 - \cos$ gusts with amplitude 15 ft/s. The gusts occur between $t = 1$ s and $t = 3$ s and last for 0.25 s each. This corresponds to a frequency of 8π rad/s. The gusts are located on the outer half of the right wing. The remainder of the aircraft does not meet any disturbance.

The antisymmetric nature of the gust field can be observed in Figure 26. A significant roll rate is achieved. Due to the high frequency of the gusts, a significant excitation of the third and fourth elastic modes is reached.

Figure 28 shows the hinge moment response of flap 16 on right and left wing. It can clearly be seen that the flap on the right wing travels through the gust field, where the additional upwash results in a negative pitching moment. The flap on the left wing is also affected by the gusts through rigid-body and elastic wing motion.
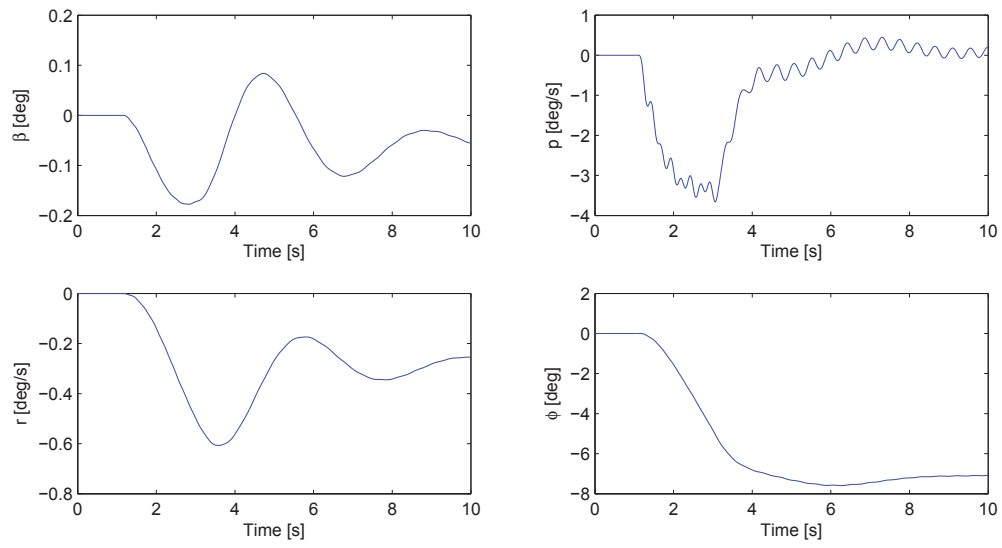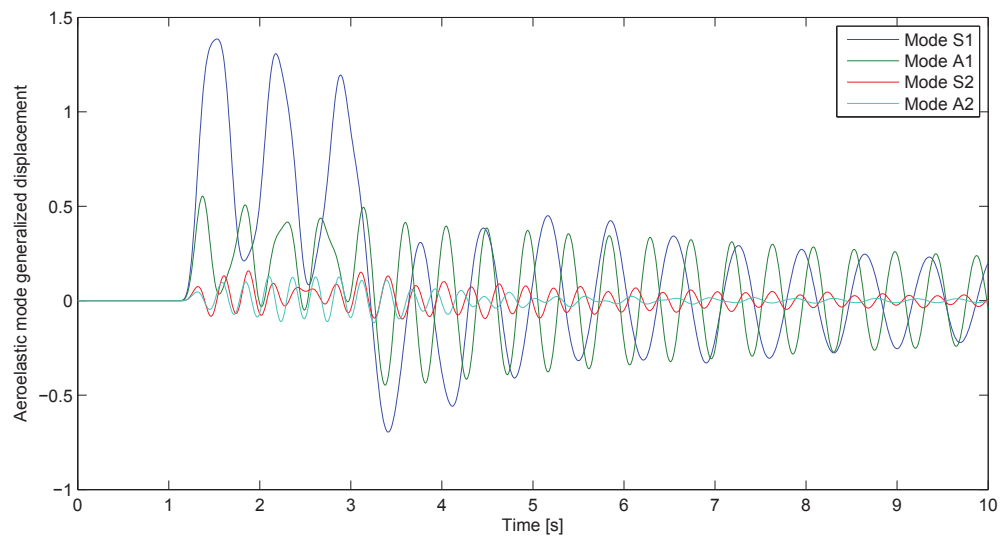
American Institute of Aeronautics and Astronautics

Figure 26: Flight dynamic gust response

Figure 27: Elastic wing gust response showing the displacement of the first four elastic modes

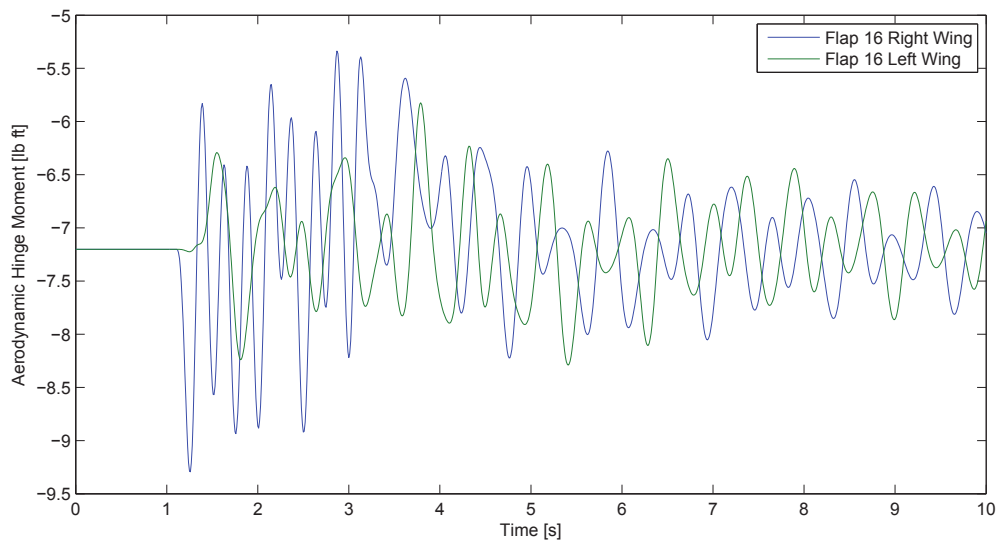American Institute of Aeronautics and Astronautics

Figure 28: Aerodynamic hinge moment response of flap 16 on right and left wing

IX. Concluding Remarks

A comprehensive flight dynamic and aeroservoelastic modeling approach for a flexible wing aircraft with VCCTEF in turbulent air was presented. Unsteady aerodynamics of the flexible wing and flap system were found using modified aerodynamic strip theory based on quasi-steady vortex-lattice results and indicial response concepts. Compressibility effects on the unsteady aerodynamics based on the work by Beddoes and Leishman et al. were taken into account throughout the modeling effort and a comparison was made with unsteady aerodynamics for incompressible flow corrected by Prandtl-Glauert compressibility correction. Simulation results, including flight dynamic and elastic responses, and aerodynamic hinge moments, were shown for flight dynamic maneuvers and gust profiles.

It was found that the modeling approach based on indicial response concepts provides a convenient manner in which quasi-steady data can be used to model the unsteady aerodynamic behavior of an aircraft with flexible wing and high-bandwidth control surfaces. Application of the indicial functions involving unsteady compressibility effects is less computationally demanding than unsteady CFD techniques and can be seen as a step in between the well-known incompressible unsteady aerodynamics function as formulated by Theodorsen and more sophisticated CFD solutions that are often computationally intensive and not well-suited for flight dynamic simulations.

X. Acknowledgment

References

[1]Nguyen, N., "Elastically Shaped Future Air Vehicle Concept," Tech. rep., NASA Innovative Partnerships Program, 2010.

[2]Nguyen, N., Trinh, K., Reynolds, K., Kless, J., Aftosmis, M., Urnes, J., and Ippolito, C., "Elastically Shaped Wing Optimization and Aircraft Concept for Improved Cruise Efficiency," *51st AIAA Aerospace Sciences Meeting*, 2013.

[3]Noll, T., Brown, J., Perez-Davis, M., Ishmael, S., Tiffany, G., and Gaier, M., "Investigation of the Helios Prototype Aircraft Mishap," Tech. rep., NASA, 2004.

[4]Theodorsen, T., "General Theory of Aerodynamic Instability and the Mechanism of Flutter," Technical Report 496, NACA, 1935.

American Institute of Aeronautics and Astronautics

[5]"AA241 Aircraft Design: Synthesis and Analysis," http://adg.stanford.edu/aa241/structures/weightstatements.html, Stanford University.

[6]Duke, E., Anoniewicz, R., and Krambeer, K., "Derivation and Definition of a Linear Aircraft Model," Reference Publication 1207, NASA, 1988.

[7]Nguyen, N., Ting, E., and Trinh, K., "Flight Dynamic Modeling and Stability Analysis of Flexible Wing Generic Transport Aircraft," *55th AIAA/ASME/ASCE/AHS/SC Structures, Structural Dynamics, and Materials Conference and Exhibit*, 2014.

[8]Sears, W. R., "Operation Methods in the Theory of Airfoils in Non-Uniform Motion," *Journal of the Franklin Institute*, Vol. 230, No. 1, 1940, pp. 95–111.

[9]Edwards, J. W., Ashley, H., and Breakwell, J. V., "Unsteady Aerodynamic Modeling for Arbitrary Motions," *AIAA Journal*, Vol. 17, No. 4, 1979, pp. 365–374.

[10]Wagner, H., "Über die Entstehung des dynamischen Auftriebes von Tragflügeln," *Zeitschrift für Angewandte Mathematik und Mechanik*, Vol. 5, No. 1, 1925, pp. 17–35.

[11]Vepa, R., "Finite State Modeling of Aeroelastic Systems," Contractor Report 2779, NASA, 1977.

[12]Tal, E., Nguyen, N., and Ting, E., "Comparison of Unsteady Aerodynamics Approximations for Time-Domain Representation of Frequency-Independent Aeroelastic State-Space Models," *56th AIAA/ASME/ASCE/AHS/SC Structures, Structural Dynamics, and Materials Conference*, 2015.

[13]Jones, R. T., "Operational Treatment of the Nonuniform-Lift Theory in Airplane Dynamics," Technical Note 667, NACA, 1938.

[14]Mazelsky, B., "Numerical Determination of Indicial Lift of a Two-Dimensional Sinking Airfoil at Subsonic Mach Numbers from Oscillatory Lift Coefficients with Calculations for Mach Number 0.7," Technical Note 2562, NACA, 1951.

[15]Bisplinghoff, R., Ashley, H., and Halfman, R., *Aeroelasticity*, Addison-Wesley Publishing Company, Inc., 1955.

[16]Lomax, H., Heaslet, M., and Sluder, L., "The Indicial Lift and Pitching Moment of a Sinking or Pitching Two-Dimensional Wing Flying at Subsonic or Supersonic Speeds," Technical Note 2403, NACA, 1951.

[17]Mazelsky, B., "Determination of Indicial Lift and Moment of a Two-Dimensional Pitching Airfoil at Subsonic Mach Numbers from Oscillatory Coefficients with Numerical Calculations for a Mach Number of 0.7," Technical Note 2613, NACA, 1952.

[18]Beddoes, T., "Practical Computation of Unsteady Lift," *Vertica*, Vol. 8, No. 1, 1984, pp. 55–71.

[19]Mazelsky, B., "On the Noncirculatory Flow About a Two-Dimensional Airfoil at Subsonic Speeds," *Journal of the Aeronautical Sciences*, Vol. 19, No. 12, 1952, pp. 848–849.

[20]Leishman, J. and Nguyen, K., "State-Space Representation of Unsteady Airfoil Behavior," *AIAA Journal*, Vol. 28, No. 5, 1990, pp. 836–844.

[21]Leishman, J., "Validation of Approximate Indicial Aerodynamic Functions for Two-Dimensional Subsonic Flow," *AIAA Journal of Aircraft*, Vol. 25, No. 10, 1988, pp. 914–922.

[22]Hariharan, N. and Leishman, J., "Unsteady Aerodynamics of a Flapped Airfoil in Subsonic Flow by Indicial Concepts," *AIAA Journal of Aircraft*, Vol. 33, No. 5, 1996, pp. 855–868.

[23]"Development of Variable Camber Continuous Trailing Edge Flap System," Report 2012X0015, Boeing, 2012.

[24]Etkin, B., "The Turbulent Wind and Its Effect on Flight," Review 44, UTIAS, 1980.

[25]Taylor, G., "The Spectrum of Turbulence," *Proceedings of the Royal Society of London A: Mathematical, Physical and Engineering Sciences*, Vol. 164, No. 919, 1938, pp. 476–490.

[26]Etkin, B., *Dynamics of Atmospheric Flight*, John Wiley & Sons, Inc., 1972.

[27]Campbell, C., "A Spatial Model of Wind Shear and Turbulence for Flight Simulation," Technical Paper 2313, NASA, 1984.

[28]*U.S. Military Handbook MIL-HDBK-1797*, US Department of Defense, 1997.

[29]Küssner, H. G., "Zusammenfassender Bericht über den instationären Auftrieb von Flügeln," *Luftfahrtforschung*, Vol. 13, No. 12, 1936, pp. 410–424.

[30]Leishman, J., "Subsonic Unsteady Aerodynamics Caused by Gusts Using the Indicial Method," *AIAA Journal of Aircraft*, Vol. 33, No. 5, 1996, pp. 869–879.

[31]Newmark, N. M., "A Method of Computation for Structural Dynamics," *American Society of Civil Engineers Journal of the Engineering Mechanics Division*, Vol. 85, No. 3, 1959, pp. 67–94.

A. Geometric Parameters

Geometric parameters with f as defined in Figure 11. Numbering according to Theodorsen is maintained.[4]

$$T_1 = -\frac{1}{3}(2 + f^2)\sqrt{1 - f^2} + f\cos^{-1} f \tag{96}$$

$$T_4 = f\sqrt{1 - f^2} - \cos^{-1} f \tag{97}$$

$$T_5 = -(1 - f^2) + 2f\sqrt{1 - f^2}\cos^{-1} f - (\cos^{-1})^2 \tag{98}$$

$$T_8 = -\frac{1}{3}(1 + 2f^2)\sqrt{1 - f^2} + f\cos^{-1} f \tag{99}$$

$$T_{10} = \sqrt{1 - f^2} + \cos^{-1} f \tag{100}$$

$$T_{11} = (2 - f)\sqrt{1 - f^2} + (1 - 2f)\cos^{-1} f \tag{101}$$

$$T_{12} = 2T_4 + T_{11} \tag{102}$$

B. Noncirculatory Flap Time Constants

Noncirculatory flap time constants according to Hariharan and Leishman.[22] The geometric property f is as defined in Figure 11, M indicates the Mach number, and β the Prandtl-Glauert factor. The $T.$ geometric coefficients are as defined in Appendix A and the circulatory coefficients are as defined in Section V.

$$K_{L_\delta} = (1 - f)\left((1 - M) + 2T_{10}\beta M^2\left(a_1^f b_1^f + a_2^f b_2^f\right)\right)^{-1} \tag{103}$$

$$K_{L_{\dot{\delta}}} = \frac{(1 - f)^2}{2}\left((1 - M)(1 - f) + T_{11}\beta M^2\left(a_1^f b_1^f + a_2^f b_2^f\right)\right)^{-1} \tag{104}$$

$$K_{m_\delta} = (1 - f)(2 + f)\left(3(1 - M) + 2\left(T_4 + T_{10}\right)\beta M^2 a_3^f b_3^f\right)^{-1} \tag{105}$$

$$K_{m_{\dot{\delta}}} = \left((1 + f)^3 - (12f - 4) - \frac{3}{2}(1 - f)^2\right)$$
$$\left(9(1 - M)(1 - f) + 6\left(T_1 - T_8 - \left(f + \frac{1}{2}\right)T_4 + \frac{T_{11}}{2}\right)\beta M^2 a_3^f b_3^f\right)^{-1} \tag{106}$$

$$K_{h_\delta} = 2\pi(1 - f)^2\left(4\pi(1 - M)(1 - f) + 4\left(T_5 - T_4 T_{10} + T_{12}T_{10}\right)\beta M^2 a_3^f b_3^f\right)^{-1} \tag{107}$$

$$K_{h_{\dot{\delta}}} = 2\pi(1 + f)^3\left(6\pi(1 - M)(1 - f)^2 + 4T_{11}(T_{12} - T_4)\beta M^2 a_3^f b_3^f\right)^{-1} \tag{108}$$

C. Aerodynamic Lift and Moment Increments

Aerodynamic lift and moment increments according to Hariharan and Leishman.[22] The geometric property f is as defined in Figure 11 and M indicates the Mach number.

$$\Delta c_{L_\delta} = \frac{2(1 - f)}{M} \tag{109}$$

$$\Delta c_{L_{\dot{\delta}}} = \frac{(1 - f)^2}{2M} \tag{110}$$

$$\Delta c_{m_\delta} = -\frac{(1 - f)(2 + f)}{2M} \tag{111}$$

$$\Delta c_{m_{\dot{\delta}}} = \frac{1}{12M}\left((1 + f)^3 - (12f - 4) - \frac{3}{2}(1 - f)^2\right) \tag{112}$$

$$\Delta c_{h_\delta} = -\frac{(1 - f)^2}{2M} \tag{113}$$

$$\Delta c_{h_{\dot{\delta}}} = -\frac{(1 - f)^3}{6M} \tag{114}$$

American Institute of Aeronautics and Astronautics